Geometric description for the anatomy of the mitral valve

Cruz De Oliveira, Diana; Srinivasan, Janaki; Espino, Daniel; Buchan, Keith; Dawson, Dana; Shepherd, Duncan

DOI:
10.1111/joa.13196

Geometric description for the anatomy of the mitral valve: A review

Authors

Diana Oliveira[a,*], Janaki Srinivasan[b], Daniel Espino[a], Keith Buchan[c], Dana Dawson[d], Duncan Shepherd[a]

[a] Department of Mechanical Engineering, University of Birmingham
Edgbaston, Birmingham
B15 2TT
* Corresponding author: DMC795@student.bham.ac.uk

[b] Cardiac Department
Aberdeen Royal Infirmary
Aberdeen
AB25 2ZN, Scotland

[c] Department of Cardiothoracic Surgery
Aberdeen Royal Infirmary
Aberdeen
AB24 2ZD, Scotland

[d] Cardiology Research Facility
University of Aberdeen and Aberdeen Royal Infirmary
Aberdeen
AB25 2ZN, Scotland

Abstract

The mitral valve is a complex anatomical structure, whose physiological-functioning relies on the biomechanical properties and structural integrity of its components. Their compromise can lead to mitral valve dysfunction, associated with morbidity and mortality. Therefore, a review on the morphometry of the mitral valve is crucial, more specifically on the importance of valve dimensions and shape for its function. This review initially provides a brief background on the anatomy and physiology of the mitral valve, followed by an analysis of the morphological information available. A characterization of mathematical descriptions of several parts of the valve is performed and the impact of different dimensions and shape changes in disease is then outlined. Finally, a section regarding future directions and recommendations for the use of morphometric information in clinical analysis of the mitral valve is established.

Keywords: biomechanics, computational anatomy, mitral valve, mitral valve disease, morphology analysis

1. Introduction

The mitral valve (MV) is one of the heart's four valves, lying between the left atrium and the left ventricle. It prevents blood from flowing backwards as it moves through the heart and it has a complex geometry, comprising the mitral annulus, the anterior and posterior leaflets and the subvalvular apparatus (Figure 1). The latter is formed by the chordae tendineae and the papillary muscles (PM), which are inserted into the left ventricular wall (McCarthy et al., 2010, Dal-Bianco and Levine, 2013). These structures work in synchrony towards its effective mechanics to enable closing and opening through the cardiac cycle (McCarthy et al., 2010).

The shape of the valve is key to many aspects of its function and disease, as identified by clinical (Lee et al., 2013, Jassar et al., 2014) studies, as well as *in silico* studies, based on either porcine (Kunzelman et al., 2007), ovine (Eckert et al., 2009) or human (Stevanella et al., 2011) models, and *in vitro* studies, based on porcine (Espino et al., 2007) and ovine (Bloodworth et al., 2017) models. Assessing its morphology can reveal various normal and abnormal features, which can be associated with deteriorating clinical outcomes (Lee et al., 2013, Sonne et al., 2009, Jolley et al., 2017, Mihaila, 2013). Moreover, the physiological-functioning of the components of the MV, as well as their ability to adapt to altered stress state imposed by the passage of blood flow, rely on their biomechanical properties and structural integrity (Al-Atabi et al., 2012, Espino et al., 2007). The success of surgical interventions (such as edge-to-edge repair or chordal replacement (Al-Atabi et al., 2012)) greatly depends on the restoration of normal fluid dynamics, which typically requires valve mechanics to be corrected (Al-Atabi et al., 2012). Thus optimising a surgical procedure, or surgical timing for MV repair, is arduous (Gao et al., 2017b). The design of medical devices for the MV is also determined by its morphometry, with a previous *in vitro* study based on porcine MVs supporting the use of saddle-shaped annuloplasty ring designs to better mimic annular shape (Jimenez et al., 2007).

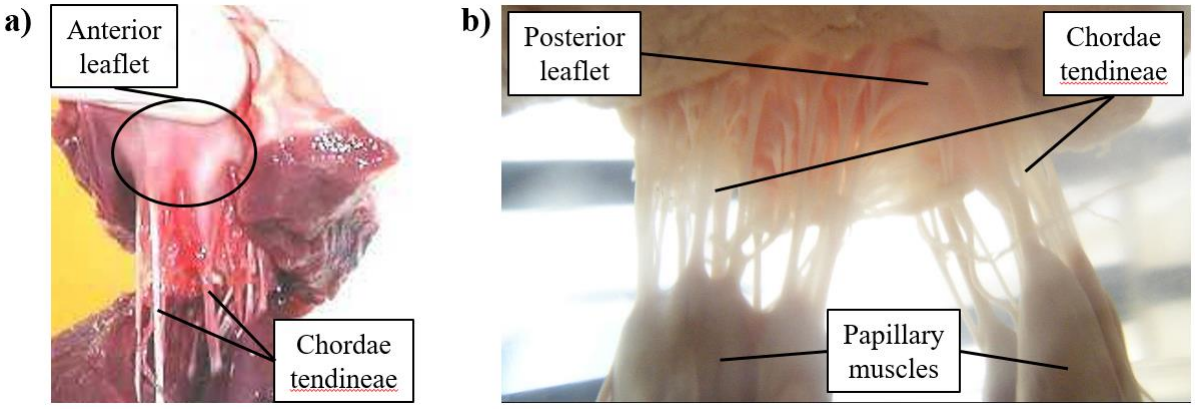

Figure 1. Porcine mitral valve apparatus: a) displays the anterior leaflet and chordae tendineae and b) focuses on the subvalvular apparatus, where chordae arise from both the PM and insert into the rough region of the posterior leaflet.

The first study reviewing the anatomic structure of the MV to identify key dimensions appeared at the beginning of the 1990s and was based on excised human and porcine MV apparatus (Kunzelman et al., 1994). This yielded basic human and porcine MV *ex vivo* measurements concerning annular and leaflet length and height, and chordal distribution. With the evolution of medical imaging modalities, *in vivo* procedures, such as three-dimensional (3D) transesophageal echocardiography, have been used to quantitatively evaluate human MV morphology in healthy and diseased cases (Lee et al., 2013, Sonne et al., 2009, Jolley et al., 2017, Mihaila, 2013, Delgado et al., 2009), proving crucial for 3D printing purposes or transcatheter MV implantation, for example. On the other hand, computational studies have mathematically represented the MV (Park et al., 2019, Salgo et al., 2002, Stevanella et al., 2009), including the annulus (Salgo et al., 2002, Stevanella et al., 2009), leaflet shape (Park et al., 2019, Stevanella et al., 2009, Shen et al., 2017), and chordae architecture (Kaiser et al., 2019) from both human and porcine dimensions and characteristics. Although many sources of MV anatomy quantification exist, a single study bringing together the current best knowledge around its morphometry, including related mathematical definitions, is lacking.

This review article aims to examine the morphometry of the MV and determine the current state of mathematical definitions of its geometrical shape. The focus is on compiling *ex vivo*/*in vivo* descriptions which are currently available in the literature to define the 3D geometry of the MV. The anatomy and physiology of the MV are briefly described, followed by mathematical definitions and morphometric information available (including associations between valve dimensions). Subsequently, a description of the impact of changes in MV morphometry in valve disease is performed and future recommendations for the use of morphometric information in MV clinical analysis are given.

2. Anatomy and physiology of the mitral valve

2.1 Mitral annulus and leaflets

The annulus is a ring of fibrous tissue that circumscribes the perimeter of the valvular orifice and the base of the valve, anchoring it within the left heart (Dal-Bianco and Levine, 2013). It is adjacent to the aortic valve, sharing a fibrous continuity with the left coronary and half of the non-coronary cusps of the aortic annulus (Veronesi et al., 2009, Ranganathan et al., 1970). This adjacent section defines the anterior portion of the mitral annulus, limited by the left and right fibrous trigones; the posterior part of the annulus is distal to the trigones and includes the lower points of its saddle shape (Dal-Bianco and Levine, 2013). Its shape and diameter vary during the cardiac cycle (Jiang et al., 2014),

making it a dynamic structure: in diastole the annulus has a more circular shape, while in systole it changes into a non-planar saddle shape in synchrony with valve closure/leaflet coaptation (Garbi and Monaghan, 2015, Al-Atabi et al., 2012, Dal-Bianco and Levine, 2013).

The leaflets of the MV are a continuous band of tissue extending from the annulus. According to their geometrical form and anatomical connection to the annulus, the leaflets are divided into anterior, posterior and commissural parts (Dal-Bianco and Levine, 2013, McCarthy et al., 2010). According to previous studies focusing on the human MV, the posterior leaflet has a semilunar shape and a relatively short radial length in comparison with the anterior leaflet, being composed of three minor semi-oval scallops: a central one opposite to the anterior leaflet, and two other, to each side (Ranganathan et al., 1970, Dal-Bianco and Levine, 2013, Carpentier et al., 1995). The anterior leaflet, on the other hand, is dome-shaped, longer and thicker (Ranganathan et al., 1970, Dal-Bianco and Levine, 2013). In systole, the free edge of both leaflets coapt, closing the valve (Ranganathan et al., 1970); in diastole, the free edges separate and the valve opens (McCarthy et al., 2010). Tissue characteristics of both leaflets also change accordingly to region, as stated by previous human mitral valve studies and as displayed in Figure 2: while the central portion is thinner and smoother (clear zone), towards the free edges (coaptation region) the tissue becomes thicker and rougher (rough zone) (Al-Atabi et al., 2012, Dal-Bianco and Levine, 2013, McCarthy et al., 2010): this is the main area of chordae tendineae attachment (Lam et al., 1970, Dal-Bianco and Levine, 2013). The posterior leaflet also possesses a chordae attachment area near the annulus, named the basal zone (Lam et al., 1970). Both leaflets consist of four histological layers: the uppermost one adjacent to the left atrium is the atrialis, composed of mainly aligned elastic/collagen fibres; beneath the atrialis is the spongiosa, which consists of an extracellular matrix of proteoglycans and glycosaminglycans, along with elastic fibres, comprising the majority of the free edge; beneath the spongiosa is the fibrosa, a major load-bearing layer forming the central structural collagenous core of each leaflet, with aligned collagen fibres; finally, the ventricularis layer is covered by a continuous sheet of endothelial cells folded with elastic and collagen fibres (McCarthy et al., 2010).

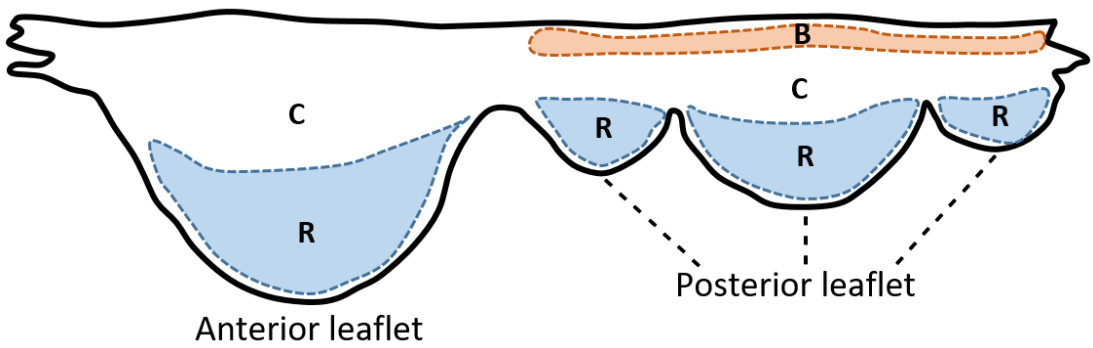

Figure 2. Human MV leaflet tissue areas. Notes: C, clear zone; R, rough zone; B, basal zone.

2.2 Subvalvular apparatus

The chordae are chord-like structures that arise from the tip of either of the two PM and insert into the leaflets (Lam et al., 1970, Al-Atabi et al., 2012). The two PMs are known as anterolateral and posteromedial, relative to the anterior and lateral body orientations and indicating the anatomical parts of the left ventricular wall into which they insert. Similarly to the mitral annulus, they are dynamic structures that move through the cardiac cycle. However, their role is unclear in the literature: previous studies focusing on dog mitral valves state that PM contraction/shortening assists in opening the MV and their elongation aids in coaptation (Marzilli et al., 1980) or that MV closing relies on PM contraction instead (Hirakawa et al., 1977). The chordae themselves are characterized according to their point of attachment and size: in a human MV, the marginal chordae are thinnest and attach to the free edge of the leaflets; basal chordae are thicker and more extensible, inserting between the free edges and the leaflet's attachment to the annulus (rough zone).

There are two thick basal chords (strut chordae) that arise from the tip of each PM and insert into the anterior leaflet: these are the largest and thickest of all chordae, carrying also the highest tension (Al-Atabi et al., 2012, Lam et al., 1970, Dal-Bianco and Levine, 2013, Lomholt et al., 2002, Wilcox et al., 2014). Their insertion region into the anterior leaflet experiences varying stretch during the cardiac cycle, which demonstrates a transfer of forces from the leaflets to the chordae and vice versa and aids in valve function (Padala et al., 2010). There are also tertiary chordae, which originate at the left ventricular wall and connect to the basal region of the posterior leaflet (Al-Atabi et al., 2012, McCarthy et al., 2010). According to porcine and ovine studies, different types of chordae have different functions: while marginal chordae maintain the leaflets closed during systole, averting regurgitation, basal chordae support and transfer loads to the leaflets, carrying also higher loads to protect marginal chordae from failure (Espino et al., 2005, Timek et al., 2001, Nielsen et al., 2003, Sedransk et al., 2002, Wilcox et al., 2014).

3. Insights into mitral valve morphometry

3.1 Mitral valve key landmarks and morphometric data

Mathematical algorithms that automatically generate parametric 3D human MV models have been developed from *in vivo* echocardiographic data (Grbic et al., 2017), four-dimensional computed tomography images (Ionasec et al., 2010) and 3D transesophageal echocardiography (Mansi et al., 2012, Zhang et al., 2017). Despite the creation of patient-specific geometries, these frameworks rely on common anatomic MV landmarks (Figure 3), from which parametric surfaces corresponding to the

mitral leaflets can be generated. These include: the left and right trigones, situated at the fibrous border between the mitral and aortic valves (Veronesi et al., 2009); the anterolateral and posteromedial commissures, located at the free edges, which are the interconnection points of the leaflets (McCarthy et al., 2010); the leaflet tips, corresponding to the line of each leaflet free-edge (Ionasec et al., 2010, Mansi et al., 2012); the posterior annular midpoint; and the PM tips (Ionasec et al., 2010, Mansi et al., 2012).

Both *ex vivo* and *in vivo* studies defined parameters that describe the human MV geometrical shape and are vital to its function. These are discretized in Table 1, and ranges of values for healthy and diseased valves are provided.

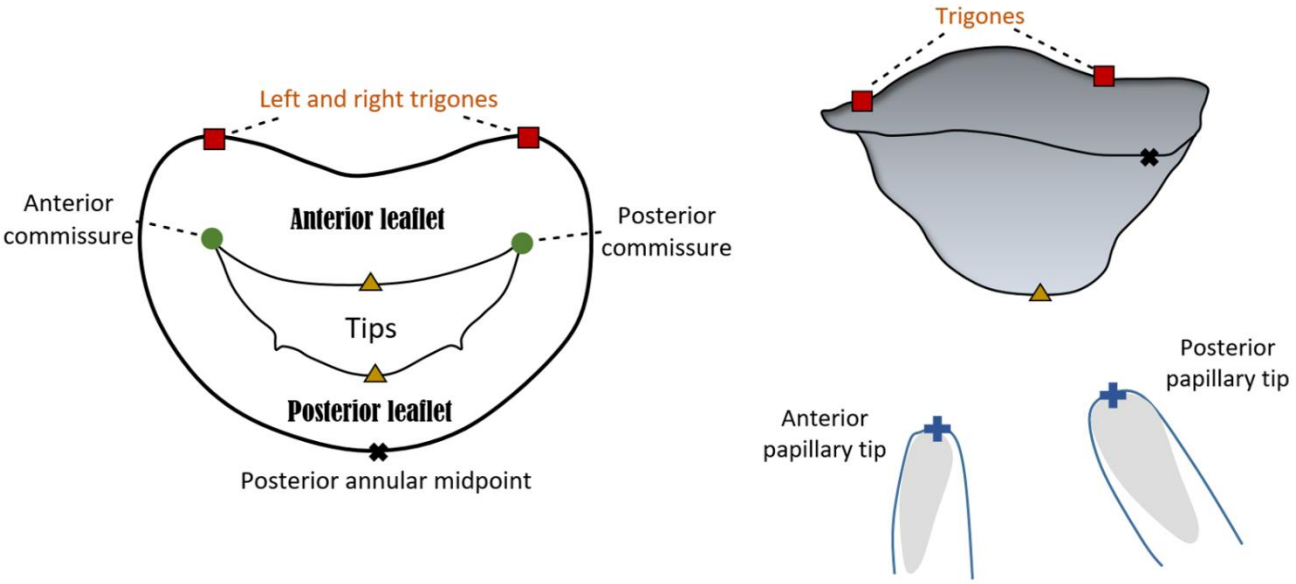

Figure 3. Atrial and lateral views of a MV schematic model based upon nine landmarks. The annulus, anterior and posterior leaflets and papillary muscle tips can be observed.

3.2 Annular proportions and saddle shape: geometrical relationships

The geometrical components of the annulus including annular anterior and posterior areas, the antero-posterior (AP), the anterolateral-posteromedial (AL-PM) and the inter-trigonal distances, represented in Figure 4a, vary over the cardiac cycle (Jiang et al., 2014). Both anterior and posterior annular portions contribute to changes in mitral annular area: although standard literature refers to annular contraction as occurring during systole, as stated in a previous ovine study (Rausch et al., 2011), there are studies based on human MVs showing annular expansion from mid-systole to early-diastole and contraction between mid-diastole and early-systole (Jiang et al., 2014, Levack et al., 2012). In addition, an in vivo study based on ovine MVs providing showed the presence of dynamic annular strain, with

the largest strains belonging to the posterior region and the commissural regions showing the least amount of variation (Eckert et al., 2009).

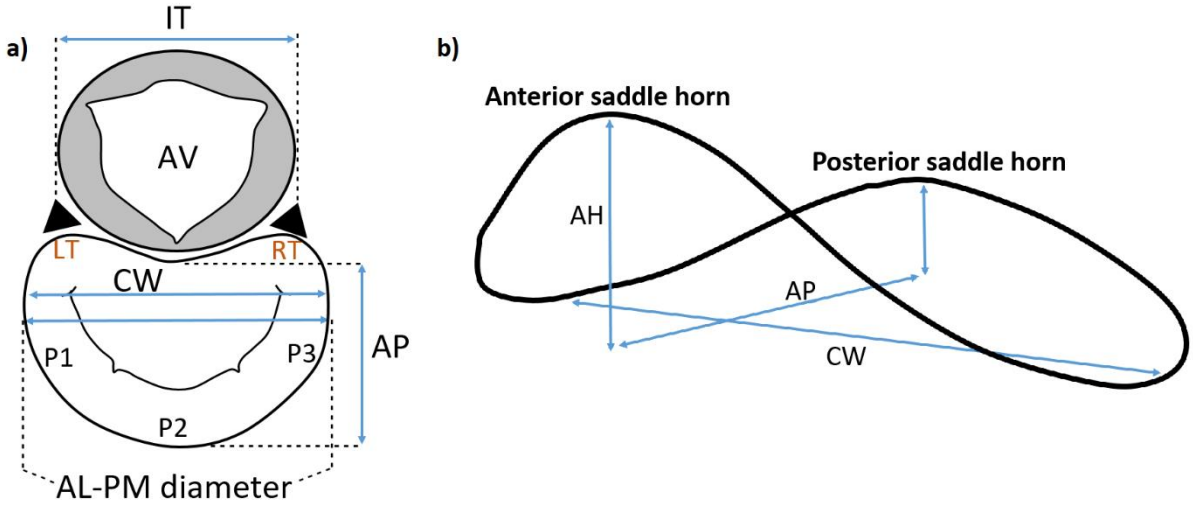

Figure 4. Atrial (a) and lateral (b) views of important mitral annular dimensions. Notes: AV, aortic valve; LT, left trigone; RT, right trigone; P1, P2, P3, posterior leaflet scallops; AL-PM diameter, anterolateral-posteromedial diameter; AP, antero-posterior distance; CW, commissural width; IT, inter-trigonal distance.

Despite this dynamic variability, the proportion concerning anterior and posterior annular circumferences in the human MV remains practically unchanged. This proportion is contradictory in the literature: while some studies mention that the anterior and posterior parts correspond to about 1/3 and 2/3 of the total annular perimeter (Garbi and Monaghan, 2015), others yield a proportionality of about 2/5 and 3/5, respectively (Pouch et al., 2014, Jassar et al., 2014). However, this proportion depends on the assumed division between leaflets, which is usually considered at the commissural level. Nonetheless, other studies divide the leaflets at the lowest annular height. The correct proportion is reflected in the literature values (obtained at mid-systole) present in Table 1 (Pouch et al., 2014, Jassar et al., 2014) and is described quantitatively by equations 1 and 2,

$$P_{AC} = 3/5 \cdot A_C \quad (1)$$

$$A_{AC} = 2/5 \cdot A_C, \quad (2)$$

where A_C is the total annular circumference and P_{AC} and A_{AC} are the posterior and anterior annular circumferences, respectively. Moreover, these proportions are firmed by correlations found in the literature, based upon dimensional data retrieved during intra-cardiac operations and dissection of fresh human hearts (Duplessis and Marchand, 1964). These yielded equations 3 ($R^2 = 0.72$, p-value < 0.01) and 4 ($R^2 = 0.93$, p-value < 0.01),

$$A_{AC} = 4.137 + 0.305 \cdot A_C, \quad (3)$$

where the A_C and A_{AC} are in mm,

$$P_{AC} = -4.137 + 0.695 \cdot A_C, \quad (4)$$

where the A_C and P_{AC} are in mm. The correlation from equation (4) was further validated through a 2D echocardiographic study concerning imaging data from 15 healthy subjects and performed by the authors. Valvar dimensions were obtained at end systole and generated a moderate correlation between the A_C and P_{AC} ($R^2 = 0.674$, p-value < 0.01). The methodology employed for equation prediction generation, as well as further characteristics of the correlations found on our study, are present in the Supplementary material.

An *ex-vivo* human study, performed within 6 hours of MV removal, examined MV geometry by assuming the mitral annulus as a circle and the A_{AC} and P_{AC} as arc lengths. This work also underlined positive linear relationships between these dimensions and the mitral annular diameter (or AL-PM distance), as given by equations 5 ($R^2 = 0.66$, p-value < 0.01) and 6 ($R^2 = 0.91$, p-value < 0.01) (Okamoto et al., 2007):

$$A_{AC} = 2.500 + 0.420 \cdot \gamma, \quad (5)$$

where γ represents the AL-PM distance and both variables are in cm,

$$P_{AC} = 4.400 + 1.200 \cdot \gamma, \quad (6)$$

where both variables are in cm. For equations 5 and 6, γ is expressed as a dimensionless Z-value in agreement with Okamoto *et al.* (2007). Further, the authors of this study have mathematically defined the A_{AC}, P_{AC} and IT distance, assuming the annulus as divided into anterior and posterior portions by the left and right trigones or commissures, as represented in Figure 5.

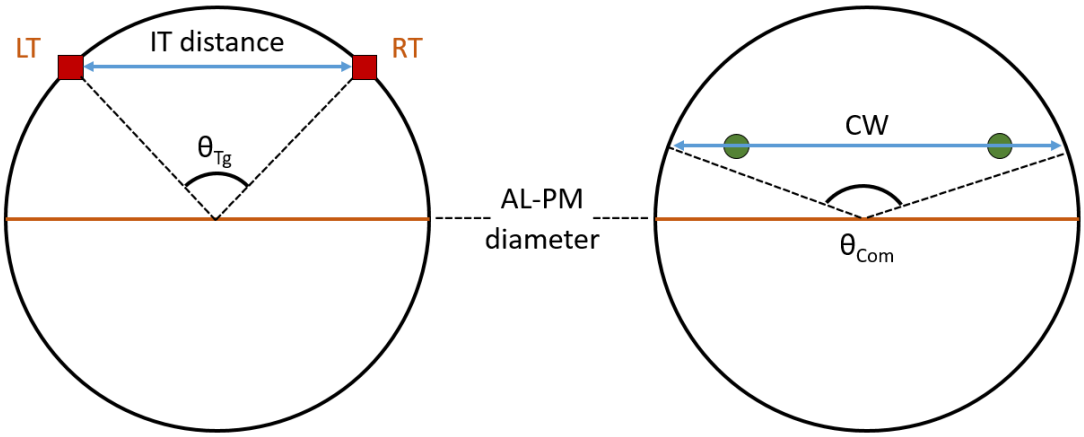

Figure 5. Circle representing the annulus, according to Okamoto *et al.* (2007), with relevant dimensions highlighted. Notes: LT, left trigone; RT, right trigone; AL-PM diameter, anterolateral-posteromedial diameter; CW, commissural width; IT distance, inter-trigonal distance; θ_{Tg}, trigonal angle; θ_{Com}, commissural angle.

Equations 7, 8 and 9 represent the mathematical definitions employed by Okamoto *et al.* (2007),

$$\mathrm{IT} = 2 \cdot \gamma \cdot \sin\left(\frac{\theta_{Tg}}{2}\right), \tag{7}$$

$$\mathrm{A_{AC}} = \pi \cdot \gamma \cdot \theta_{Tg} \cdot \theta_{Com}, \tag{8}$$

$$\mathrm{P_{AC}} = \pi \cdot \gamma \cdot (360 - \theta_{Tg} \cdot \theta_{Com})/360, \tag{9}$$

where IT is the inter-trigonal distance, γ is the AL-PM distance, θ_{Tg} is the angle between left and right trigones and θ_{Com} is the angle between commissures at the annular plane (Okamoto et al., 2007). However, these definitions simplify the shape of the anterior leaflet to great extent and do not accurately represent its real configuration.

An association between the annular circumference and the total leaflet free edge length has also been found based on the *ex vivo* human MV data from Duplessis *et al.* (1964). Greater total and posterior annular circumferences were moderately correlated with increased free edge lengths, as provided in the equations below,

$$\delta = 18.824 + 0.704 \cdot \mathrm{A_C}, \tag{10}$$

where δ represents the free edge length, and both variables are in mm ($R^2 = 0.76$, p-value < 0.01),

$$\delta = 26.301 + 0.964 \cdot \mathrm{P_{AC}}, \tag{11}$$

where both variables are in mm ($R^2 = 0.74$, p-value < 0.01),

Annular shape is distinctive due to its similarity with a saddle, being characterized by an annular height (AH) (Figure 4b). This is characteristic of a healthy valve, as it reduces leaflet stress and decreases anterior systolic strain, potentially increasing repair durability (Salgo et al., 2002, Jimenez et al., 2007). In practice, a deeper saddle relates to more apical positions of the medial and lateral aspects of the annulus, while the anterior and posterior aspects remain basal (Salgo et al., 2002). This is mathematically described by the annular height to commissural width ratio (AHCWR), which provides with a quantitative measure of annular nonplanarity (Lee et al., 2013, Pouch et al., 2014, Jassar et al., 2014). According to this, we can also define the AHCWR as

$$\varepsilon = AH/AP \cdot CI, \tag{12}$$

where ε represents the AHCWR, AH is the annular height, AP is the antero-posterior distance and CI is the circularity index. The latter is defined as the ratio between the AP diameter and the commissural width (CW) and accounts for the greater or smaller ellipsoidal shape of the annulus (Lee et al., 2013, Pouch et al., 2014).

The human MV AHCWR profile depends on the rotational position of the annulus, and has led to the generation of new annuloplasty ring designs (Pouch et al., 2014, Jassar et al., 2014). In fact, saddle shape variability impacts on leaflet stress variation (Salgo et al., 2002): a deeper saddle shape, associated with a higher AHCWR percentage (Lee et al., 2013), leads to leaflet peak stress reduction, as predicted by computational studies (Salgo et al., 2002). Further, geometric correlations concerning the AL-PM distance and other mitral annular dimensions have been found both in the literature and in our 2D echocardiographic study. For example, a clinical 3D transesophageal echocardiography study focusing on the end-systolic frame yielded that lower non-planarity angles (NPA) were associated with increased AH to the AL-PM distance ratios, as given by equation 13 ($R^2 = 0.70$, p-value < 0.01) (Warraich et al., 2012),

$$NPA = 179.600 - 163.900 \cdot \sigma, \tag{13}$$

where σ represents the AH to the AL-PM distance ratio (dimensionless) and the NPA is in º. A moderate association between the ratio of the AH to the AL-PM distance and the ratio of the AH to the AP distance was also found ($R^2 = 0.78$, p-value < 0.01) (Warraich et al., 2012):

$$\sigma = 0.027 + 0.970 \cdot \tau, \quad (14)$$

where τ represents the AH to the AP distance ratio. Nonetheless, given mitral annular dynamic shape changes through the cardiac cycle (the AH suffers a total percentage change of 13.5±7.8 in the cardiac cycle, for example (Tang et al., 2019)), we cannot assume that the relationships afore mentioned are maintained both in systole and in diastole.

Our 2D echocardiographic study revealed a moderate association between the AL-PM distance and the inter-trigonal distance at end-systole, displayed in equation 15 ($R^2 = 0.65$, p-value < 0.01):

$$IT = 19.280 \cdot e^{(0.017 \cdot \gamma)} \quad (15)$$

where IT represents the inter-trigonal distance and both variables are in mm.

The AP distance is also geometrically associated with other annular parameters in the human MV. Equations 16 and 17 present moderate correlations between the ratio of the AH to the AP distance and the NPA ($R^2 = 0.64$, p-value < 0.01) and between the 2D annular area and the AP distance ($R^2 = 0.65$, p-value < 0.01), respectively, generated with data obtained at end-systole:

$$NPA = 177.580 - 142.880 \cdot \tau, \quad (16)$$

where τ is dimensionless and the NPA is in º,

$$AP = 18.206 + 0.016 \cdot A_{na}, \quad (17)$$

where A_{na} is the annular area in mm^2 and AP is in mm.

The annular saddle shape has been mathematically defined through paraboloid equations, which are quadric surfaces with one axis of symmetry and no centre of symmetry (Salgo et al., 2002, Stevanella et al., 2009, Park et al., 2019). In Salgo *et al.* (2002), for example, hyperbolic paraboloids were employed (Salgo et al., 2002), while Park *et al*. used hyperbolic paraboloids for the saddle shape definition. In addition, they designed a ring-shaped structure, mathematically described as a curved toroid and with empirical relationships derived below (Park et al., 2019),

$$z = \frac{(x - \alpha_L)^2}{a \cdot \alpha_V} - \frac{(y - \beta_L)^2}{b \cdot \beta_V}, \quad (18)$$

MV component	Geometric variables	Meaning	Ranges	
			Healthy	Diseased
Annulus	AP diameter [mm]	Distance between anterior and posterior annular midpoints	30±6*	38.8±6.4†
	CW [mm]	Annular diameter at the commissures	33.3±3.7†	42.2±5.9†
	AL-PM diameter [mm]	Diameter between anterolateral and posteromedial landmarks	31±5*	39±7*
	Annular circumference [mm]	Total perimeter of the annular edge	106±10†	136±19†
	Anterior/posterior circumferences [mm]	Perimeter of the anterior/posterior annular edges	Anterior: 43.3±8.2* Posterior: 63.01±9.06*	Anterior: 61.3±8* Posterior: 75±11*
	Annular height [mm]	Vertical distance between highest and lowest annular points	7.9±1.9†	5.6±1.6†
	Annular area [mm^2]	Area enclosed by the 2D projection of the annulus	780±270*	1343±392†
	NPA [°]	Angle between anterior and posterior annular midpoints at the commissure	144±11*	157±12*
	IT distance [mm]	Distance between left and right trigones	30±3‡	31±3‡
Leaflets	Anterior/posterior lengths [mm]	Length from anterior/posterior annular midpoints to coaptation	Anterior: 21.2±3.0† Posterior: 9.8±2.0†	Anterior: 26.3±6.1† Posterior: 16±5†
	Anterior/posterior areas [mm^2]	Surface area of anterior/posterior leaflets	Anterior: 530±210* Posterior: 380±130*	Anterior: 760±190* Posterior: 610±230*
	Posterior scallop lengths [mm]	Length from each scallop free margin to annulus	P1: 5-17; P2: 7-20; P3: 7-20※	P1: 16±5; P2: 19±6; P3: 16±4*
	Commissural heights [mm]	Height from each commissural free margin to annulus	AL: 5-13; PM: 4-12※	----------
	Leaflet angles [°]	Angle created by the anterior/posterior leaflets with the annulus line	Anterior: 24.6±7* Posterior: 34.7±9.6*	Anterior: 33.2±8.6* Posterior: 44.4±11.9*
	Tenting height [mm]	Distance from the annulus to coaptation	7.4±1.3⁑	9.7±3.2*
	Tenting area [mm^2]	Silhouette delineated by leaflets from annulus to coaptation	118.2±32.6⁑	350±50⁑
Subvalvular apparatus	PM length [mm]	Length from each PM to anterior annular midpoint	ALPM: 28.1±4.1† PMPM: 28.5±4.8†	ALPM: 40.5±6† PMPM: 41.8±5.9†
	Inter-papillary distance [mm]	Distance between PMs	Inner: 14.4±4.8* Outer: 31.1±5.4*	Inner: 26.7±8.4* Outer: 43.1±9.7*
	Inter-papillary angle [°]	Angle between anterior annular midpoint to both PMs	26.2±6.5‡	28.9±6.3‡

Table 1. Geometric variables of the MV and healthy and diseased (significant regurgitation) literature ranges ((Lee et al., 2013, Mihaila, 2013, Machino-Ohtsuka et al., 2016, Obase et al., 2016, Deorsola and Bellone, 2018, Jassar et al., 2014, Calleja et al., 2015, Sonne et al., 2009, Pouch et al., 2014, Jiang et al., 2014, Suri et al., 2009, Owais et al., 2016, Kunzelman et al., 1994, Ranganathan et al., 1970, Delgado et al., 2009, Dudzinski and Hung, 2014, Yamaura, 2008, Kim et al., 2014, Topilsky et al., 2013)). Dimensions obtained at: ⁑, early systole; *, mid-systole; †, end-systole; ‡, averaged over cardiac cycle; ※, *ex vivo*. Notes: AP, antero-posterior; CW, commissural width; AL-PM, anterolateral-posteromedial; NPA, non-planarity angle; IT, inter-trigonal; PM, papillary muscle; P1, posteromedial commissural scallop; P2, posterior middle scallop; P3, anterolateral commissural posterior scallop; AL, anterolateral; PM, posteromedial; ALPM, anterolateral papillary muscle; PMPM, posteromedial papillary muscle.

where α_L and β_L are transformation parameters in lateral directions in the xy plane that define the saddle point, α_V is a transformation parameter in the vertical direction in the xz plane and β_V is the transformation parameter in the vertical direction in the yz plane. These parameters vary between 0 and 1) and a and b are determined by annular dimensions,

$$a = \frac{(\gamma)^2}{4 \cdot AH} \tag{19}$$

$$b = \frac{(AP)^2}{4 \cdot AH} \tag{20}$$

Equation 18 allows the manipulation of lateral and vertical curve transformations representative of changes in saddle depth and commissural height, for example (see Figure 6).

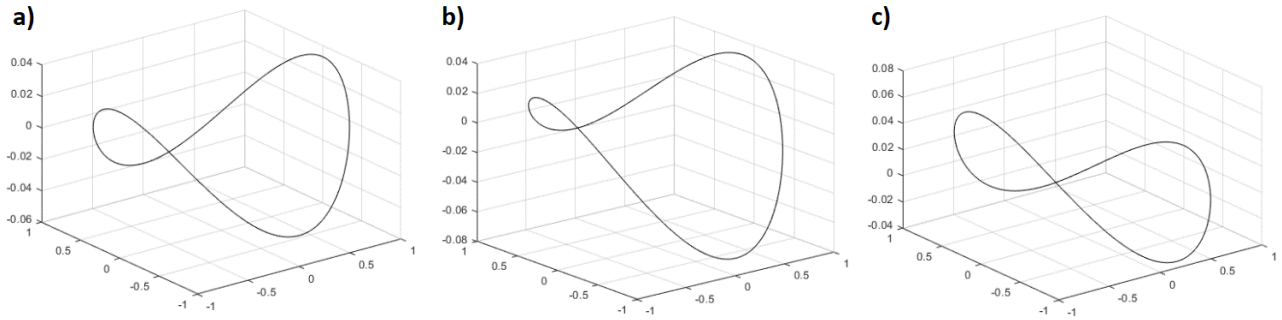

Figure 6. Hyperboloids representing the MV saddle shape and defined by equation 11 (Park et al., 2019) are displayed, created upon literature values for CW (33.3 mm), AP diameter (28 mm), AL-PM diameter (31 mm) and AHCWR (0.237). We can observe different commissural heights (b) and posterior annular depth (c) in comparison with a pure hyperboloid (a), given by changes in transformation parameters.

The NPA is not the only factor influencing annular saddling: the leaflet angles (α_A, and α_P, represented in Figure 7) and the overall coaptation triangle (2D triangle formed by the AP diameter, anterior and posterior leaflets when the leaflets coapt), including tenting height and tenting area, also play an important role in the evaluation of human MV geometry and function (Deorsola and Bellone, 2018, Delgado et al., 2009, Silbiger, 2011, Ciarka et al., 2010). A schematic of this coaptation triangle is represented in Figure 7, as well as related linear and angular dimensions. A previous study hypothesized that the coaptation triangle of healthy valves could be based on the Golden Proportion, a ratio observed in Nature which derives from sectioning a certain segment in two different parts (Deorsola and Bellone, 2018). Such ratios yield an irrational number (rounded to 0.618 or 1.618) known as the Golden Proportion. This study states that the value of 0.618 can be obtained through the ratio between the anterior cord and the AP diameter, between the posterior and the anterior cords and between the tenting height and the posterior cord.

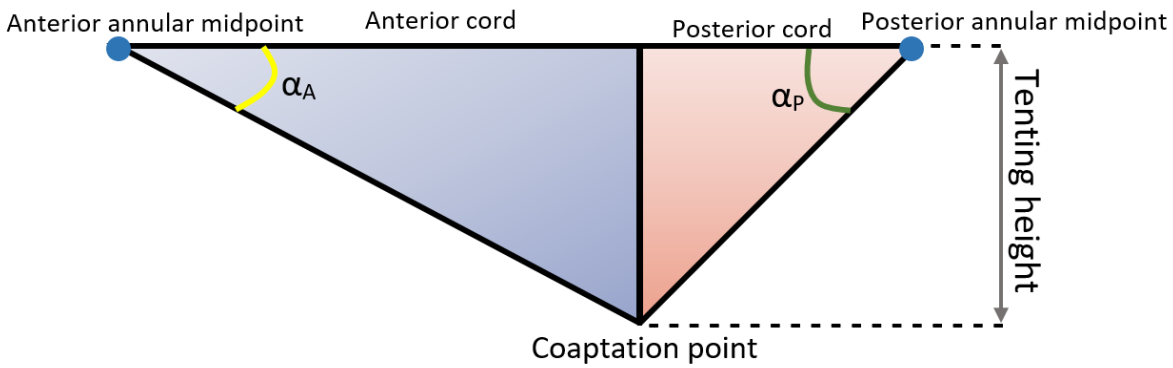

Figure 7. Coaptation triangle. The tenting height divides the base of the triangle (AP diameter) into two segments – the anterior and the posterior cords. Notes: α_A, anterior leaflet angle; α_P, posterior leaflet angle.

Indeed, Deorsola *et al*. found strong correlations between the original coaptation triangle and the Golden (or mathematical) one at early systole (time point of measurements), showing good positive linear relationships between the AP diameter and the anterior cord (equation 21, $R^2 = 0.97$, p-value < 0.01) and between anterior and posterior cords (equation 22, $R^2 = 0.82$, p-value < 0.01).

$$A_{cord} = 1.391 + 0.580 \cdot AP, \quad (21)$$

where the AP diameter and A_{cord} (anterior cord) are in mm,

$$P_{cord} = -1.279 + 0.667 \cdot A_{cord}, \quad (22)$$

where the A_{cord} and P_{cord} (posterior cord) are in mm. Unfortunately, Deorsola *et al*. mention that, due to technical imaging limitations, they were unable to assess the coaptation triangle and repeat measurements for each frame of the cardiac cycle, determining whether the Golden Proportion or the correlations found would be maintained both in systole and diastole (Deorsola and Bellone, 2018). Nonetheless, the anterior and posterior leaflet angles are an important element for the evaluation of leaflet tethering, with a posterior leaflet angle of 45 degrees or above being an index of severe leaflet tethering in ischemic mitral regurgitation. In fact, a previous study found that a P3 tethering angle below 28.8 degrees would predict the improvement of this type of regurgitation after surgery (Bouma and Gorman, 2019, Sun et al., 2019). From a diagnostic and surgical point of view, this means that leaflet angles could represent important parameters to identify early anatomical alterations or to improve surgical strategy and postoperative evaluation, especially when correlated with other MV dimensions of the coaptation triangle (Deorsola and Bellone, 2018).

3.3 Leaflet dimensions and shape

Figure 8 shows anterior and posterior leaflet heights and lengths, as well as commissural length and leaflet area for a generic human MV.

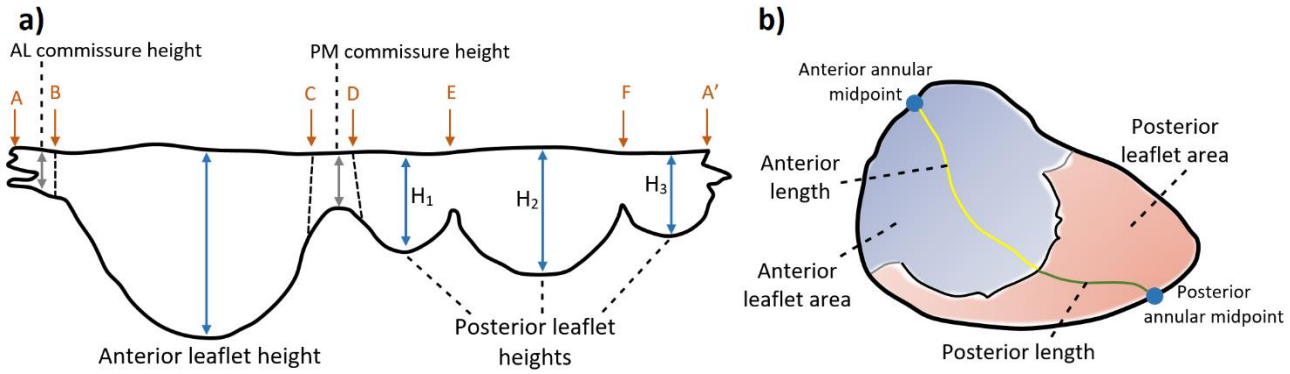

Figure 8. Parameters of human MV leaflet geometry, with an extended (a) and closed (b) leaflet representation. Notes: A-B, anterolateral commissure; B-C, anterior leaflet; C-D, posteromedial commissure; D-A', posterior leaflet; D-E, posteromedial commissural scallop (P1); E-F, middle scallop (P2); F-A', anterolateral commissural scallop (P3).

Geometrical associations concerning the anterior leaflet have been determined from *ex vivo* human data from Duplessis *et al.* (1964). Dependencies between anterior leaflet surface area and other dimensions of the valve were discovered: correlations are present between this area and the A_C (equation 23, $R^2 = 0.70$, p-value < 0.01) and A_{AC} (equation 24, $R^2 = 0.81$, p-value < 0.01); and a moderate correlation between this area and the free edge lengths (equation 25, $R^2 = 0.62$, p-value < 0.01),

$$A_{LA} = 127.300 + 3.549 \cdot A_C, \tag{23}$$

where A_{LA} is the anterior leaflet surface area (in mm^2) and the A_C is in mm,

$$A_{LA} = 114.830 + 10.630 \cdot A_{AC}, \tag{24}$$

where the A_{AC} is in mm and the A_{LA} is in mm^2,

$$\delta = 17.840 + 0.150 \cdot A_{LA}, \tag{25}$$

where the A_{LA} is in mm^2 and δ is in mm (Duplessis and Marchand, 1964).

Similarly, further human *ex vivo* correlations between the posterior leaflet surface area and other dimensions of the valve were obtained from Duplessis *et al*. (1964), including: good associations with

the A_C (equation 26, $R^2 = 0.85$, p-value < 0.01) and with the P_{AC} (equation 27, $R^2 = 0.82$, p-value < 0.01) and a moderate association with the free edge length (equation 28, $R^2 = 0.75$, p-value < 0.01),

$$P_{LA} = 65.749 + 4.262 \cdot A_C, \quad (26)$$

where P_{LA} is the posterior leaflet surface area (in mm^2) and the A_C is in mm,

$$P_{LA} = 113.250 + 5.798 \cdot P_{AC}, \quad (27)$$

where the P_{AC} is in mm and the P_{LA} is in mm^2,

$$\delta = 14.797 + 0.152 \cdot P_{LA}, \quad (28)$$

where the P_{LA} is in mm^2 and δ is in mm (Duplessis and Marchand, 1964).

In addition, a moderate correlation between anterior and posterior leaflet surface areas was also discovered from the data from Duplessis *et al.* (1964) (Duplessis and Marchand, 1964) (equation 29, $R^2 = 0.71$, p-value < 0.01),

$$P_{LA} = 53.285 + 0.914 \cdot A_{LA}, \quad (29)$$

where the A_{LA} and P_{LA} are in mm^2 (Duplessis and Marchand, 1964).

The posterior leaflet has been mathematically characterized as a continuous shape around the annulus, with (Stevanella et al., 2009, Stevanella et al., 2011, Choi et al., 2016) or without (Kunzelman et al., 1993, Cochran and Kunzelman, 1998, Kunzelman et al., 2007, Domenichini and Pedrizzetti, 2015) scallop indentations. The main focus has been given to the mathematical definition of the complete leaflets free margin. This has been generated through mathematical harmonic functions (Stevanella et al., 2009), spline functions (Stevanella et al., 2011) and parametric equations (Domenichini and Pedrizzetti, 2015). However, these frameworks simplify leaflet shape to great extent, resulting in overly idealised geometries.

Better leaflet geometrical descriptions are have been recently developed: Khaligi *et al.* (2018) built high quality 3D parametric models of MV leaflet surfaces using *ex vivo* high-resolution images from ovine MV, obtained through micro-computed tomography. They then employed quadric surfaces representing toroidal topology to create parametric large-scale models of the MV and information on the deviation between parameterized models and the original geometries to derive leaflet local thickness (Khalighi et al., 2018). Other study focused on the development of ex vivo methods to inform

on the sensitivity of model performance to the accuracy of the input geometry and to acquire comprehensive data sets to validate computational simulations against (Bloodworth et al., 2017). These works could be potentially employed on high-fidelity MV models concerning healthy, diseased and repair states; however, since it relies on images obtained through an ex vivo imaging modality, its translation to the generation of *in vivo* human MV models remains challenging.

3.4 Papillary muscle position and chordae insertion

The human PMs exhibit great morphological variability (Stevanella et al., 2011, Stevanella et al., 2009). Although two in number (Al-Atabi et al., 2012), there are usually groups of muscles adjoining, reaching a total number as high as five and attaching to the left ventricular wall either at its middle, upper or lower sections (Saha and Roy, 2018). Moreover, their shape is diversified, resembling either a cone (conical shape) or a elliptic paraboloid, having a truncated shape, or being bifurcated or trifurcated (Saha and Roy, 2018). Further, the number of chordae tendineae that attach to the PM, as well as their insertion distribution, is a source of variability. These features contribute to PM morphological heterogeneity, either in shape or attachment site. Therefore, current mathematical representations of the PM as unique points are restrictive and not accurately representative.

The PMs spatial position in humans has been mathematically defined, especially taking into account measurements such as their distance to the mitral annulus or to mitral coaptation (Yamaura, 2008, Sakai et al., 1999). Other measures of interest, such as the distance between PM or the inter-PM angle, have also been employed to describe PM morphology (Figure 9). Some studies have provided measurements of the PM to five key annular sites named o'clock points (Figure 10) (Sakai et al., 1999, Yamaura, 2008). Here, each PM is associated with three distances to the annulus, allowing the description of the 3D spatial position of their tips if assumed as a unique 3D point. More recently, another study has employed knowledge on similar measurements to build a high-resolution 3D magnetic resonance imaging apparatus, giving rise to high quality 3D models of the whole human MV structure (Stephens et al., 2017).

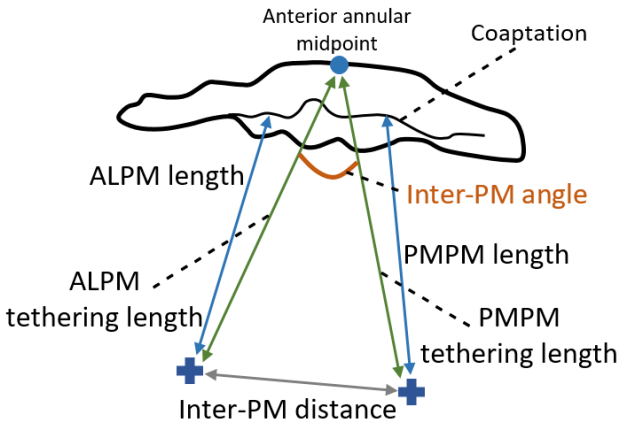

Figure 9. Measurements describing PM morphology. Notes: ALPM, anterolateral PM; PMPM, posteromedial PM.

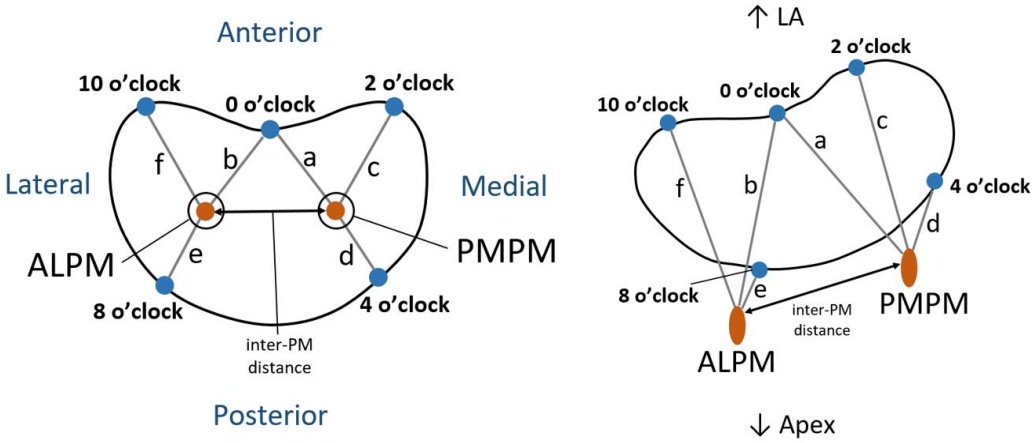

Figure 10. Distances between PM tips and o'clock points of mitral annulus, in axial (left) and isometric (right) views (adapted from (Sakai et al., 1999, Yamaura, 2008)). Notes: ALPM, anterolateral PM; PMPM, posteromedial PM; 0 o'clock, midpoint of the anterior annular circumference; 2 o'clock, right trigone; 10 o'clock, left trigone; 4 o'clock, separation of posterior and middle scallops of posterior leaflet; 8 o'clock, separation of anterior and middle scallops of posterior leaflet.

The mathematical description of human chordae tendineae remains challenging, due to the fact that their geometry is of difficult detection through common *in vivo* imaging modalities (Khalighi et al., 2017, Dal-Bianco and Levine, 2013) and meaning that human *ex vivo* studies are the primary sources of knowledge regarding chordal anatomy. Chordae tendineae are distinguished by their morphological diversity in number, insertion points into the leaflets, thickness and branching patterns, as given by previous human *ex vivo* studies (Lam et al., 1970, Gunnal et al., 2015). Regarding human MVs, it is difficult to characterize the exact insertion points of chordae into the leaflets with the current imaging techniques available (Yamaura, 2008), and even the mathematical description of the location of insertion points into the PMs and into the mitral leaflets is based upon assumptions and the expertise of clinicians (Stevanella et al., 2011).

In reality, for a human MV model representation, it is common to mathematically simplify the shape of the PMs, as well as chordae insertion patterns: some studies represent the PM tips as unique 3D points where all chordae insert, as previously mentioned (Cochran and Kunzelman, 1998, Stevanella et al., 2009, Prot et al., 2010, Rim et al., 2013); others assume a parabola representing a 2D cut-section of the PM shape, but still where all chordae insert on the tip (Park et al., 2019); and other authors assume them to have a spherical (Stevanella et al., 2011, Wang and Sun, 2013) or C (Choi et al., 2016) shape (schematized in Figure 11) and create different insertion points for the chordae according to their classification.

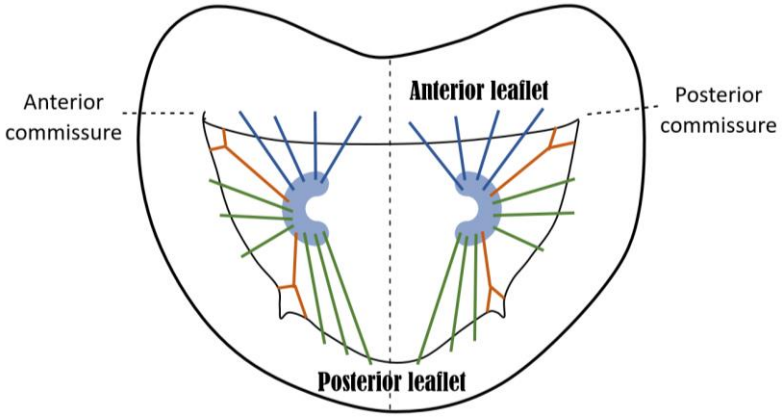

Figure 11. Axial view of C-shape representation for the PMs, as present in the literature and suggested by expert surgeons, as well as a simplified depiction of chordae tendineae insertion patterns. Blue, green and orange chordae are those inserting into the anterior leaflet, posterior leaflet and paracommissural zones, respectively.

Recent studies based on ovine MV have looked into further characterizing chordae tendineae geometry and topology (Khalighi et al., 2017), as well as evaluating how native chordal anatomic characteristics affect valvar performance (Khalighi et al., 2019). Khalighi *et al.* (2017) based their investigation on high-resolution micro-CT derived 3D models, obtaining mathematical descriptions of the chordae such as curve-skeleton characterizations, B-spline parameterizations and Reeb graph representations (see Figure 12). They used the curve-skeleton models to derive bifurcation and non-planarity angles and also analysed the spatial distribution of chordae insertion sites into the leaflets. (Khalighi et al., 2017). Their work yielded valuable information about chordal geometric characterization, including the presence of a non-homogeneous cross-sectional area along each segment (with chordal structure becoming thinner as it gets away from the PM tip); the 2D nature of chordae, which collectively form a 3D load-bearing support structure of the MV leaflets; and the development of analytical statistical models that describe chordae geometry, as well as binary trees, which aid in the prediction of possible shapes for chordal structure (Khalighi et al., 2017). Khalighi *et al.* (2019), on the other hand, found that varying cross-sectional area, branching patterns and PM insertion points at the same origin did not greatly impact in ovine MV performance and described an optimal chordae number range for

appropriate function which eliminated over 75% of the native population of chordal insertions (Khalighi et al., 2019). Both studies then shed light on chordae tendineae geometrical characterizations which can possibly be applied to develop human MV models with simplified sub-apparatus structures as a mean to overcome the current issues with in vivo imaging modalities.

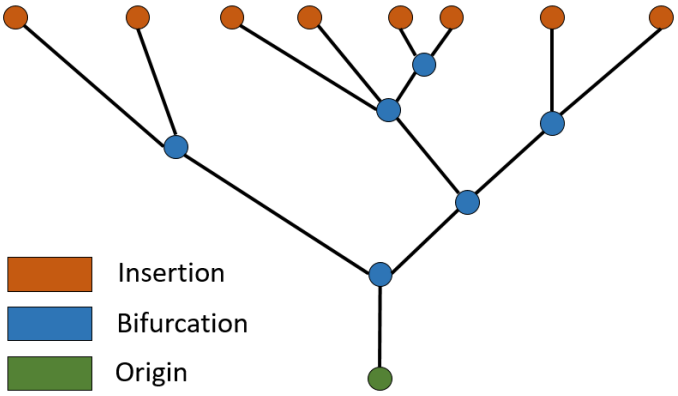

Figure 12. Example of Reeb graph employed to characterize chordae tendineae topology in Khalighi et al. (2017), illustrating the connectivity between branches. Green, blue and orange vertices correspond to chordal origin (at the PM level), bifurcation points and insertion points into the leaflets, respectively.

4. Changes in mitral valve morphometry: disease

4.1 Carpentier's functional classification of MV disease

One of the most commonly used classifications of MV disease was designed by Alain Carpentier (Carpentier, 1983), sometimes referred to as the "pathophysiologic triad" (Carpentier et al., 1980). It divides MV dysfunctions in three categories, all of which yield lesions that lead to clinical mitral regurgitation. These categories are based on the position of leaflet margins with respect to the mitral annulus plane: type I refers to normal leaflet motion and is associated with annular dilation and leaflet perforation; type II characterizes excessive leaflet motion, usually derived from elongation or rupture of the chordae tendineae and/or the PM; and type III relates to restricted leaflet motion due to retraction of the subvalvular apparatus (IIIa) or PM displacement and left ventricular dilation, causing apical displacement (tethering) of the PM (IIIb). Further information on this classification and the associated lesions can be found elsewhere (Castillo et al., 2011, Carpentier, 1983, Stone et al., 2015). Mathematical interpretations of this classification were attempted by previous studies, for example representing annular dilation by increasing its diameter or PM displacement by increasing inter-PM distance (Park et al., 2019). Taking this into account and the current literature available, examples of clinical lesions related to MV dysfunctional categories, and their influence in MV geometrical changes, are included in the following sections.

4.2 Geometrical changes in the mitral annulus are linked to type I dysfunction

In type I dysfunction, the human mitral annulus undergoes structural changes, becoming larger and flatter and losing its saddle shape (Mihaila, 2013, Lee et al., 2017). A mathematical representation of this is showed in Figure 13, where the annulus was obtained using dimensions characteristic of annular dilation, including a lower AHCWR, displayed against a healthy configuration.

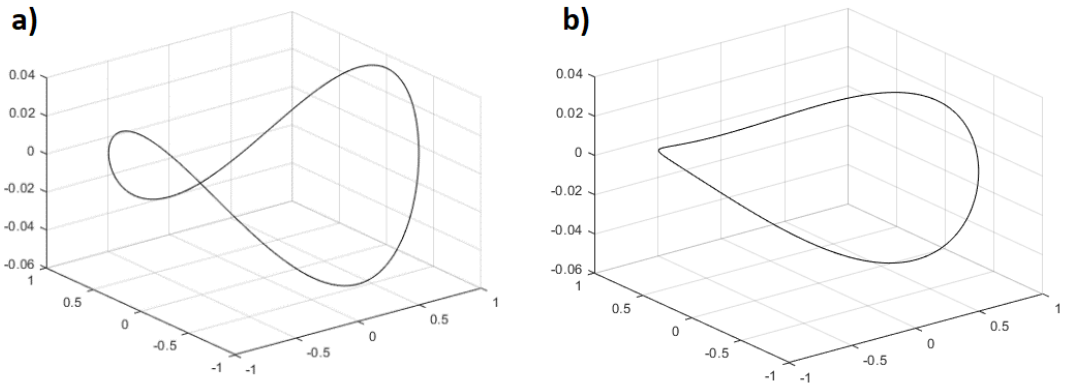

Figure 13. Hyperboloids representing: a) a mitral annular normal saddle configuration; b) a configuration associated with type I dysfunction, defined as in Park et al (Park et al., 2019). The first configuration was created with the dimensions mentioned on Figure 6 and the diseased one upon literature values for CW (42.2 mm), AP diameter (38.8 mm), AL-PM diameter (39 mm) and AHCWR (0.132).

The increase in annular size associated with this type of mitral dysfunction compromises leaflet coaptation length and therefore prevents proper valve closing (Silbiger, 2011). For example, a previous *in vitro* study based on porcine MV showed that increasing annular area values (annular dilation) were associated with a decrease in the pressures needed to cause MV failure (Espino et al., 2007). The association between the effective regurgitant orifice area (EROA) and MV geometry serves as a validation of the role played by abnormalities in shape in dysfunctional cases. Concerning the human MV, increases in this index, linked to greater severity of regurgitation, have been associated with increasing annular circumference and area at end-systole, although such associations were poorly correlated (R^2 = 0.38, R^2 = 0.48, respectively, with p-value < 0.01) (Cong et al., 2018). Lee *et al*. (2013) have also seen an inverse correlation between EROA and AHCWR at the same time frame, showing loss of MV saddle shape with increasing regurgitation (R^2 = 0.44, p-value < 0.01) (Lee et al., 2013).

Other clinical studies have also correlated an increase in EROA with greater non-coaptation distance between leaflets (maximal distance between both leaflet edges) at end-systole, as given by equation 30 (R^2 = 0.68, p-value < 0.01) (Senechal et al., 2012),

$$\lambda = 0.066 \cdot e^{(0.325 \cdot \mu)}, \quad (30)$$

where μ represents the non-coaptation distance (in mm) and λ represents the EROA (in cm^2).

In vivo human studies show that the flattening in MV shape present in disease is associated with loss of nonplanarity (Silbiger, 2011, Lee et al., 2013), quantified by increased NPAs (Mihaila, 2013), and greater billowing, showed as a correlation between lower AHCWR and higher values of billow volume ($R^2 = 0.66$, p-value < 0.01) obtained at end-systole,

$$BV = 10.000 - 0.792 \cdot \varepsilon + 0.016 \cdot \varepsilon^2, \quad (31)$$

where BV represented the billow volume (ml) and ε represents the AHCWR (as a percentage) (Lee et al., 2013).

In vivo studies have also showed a change in individual measurements describing annular shape in diseased cases: the AP diameter has been shown to increase in regurgitant valves (Lee et al., 2013, Mihaila, 2013), as well as the AL-PM diameter (Mihaila, 2013) and the commissural width (Lee et al., 2013). In addition, greater values of the circularity index are present in cases of regurgitation (Lee et al., 2013), associated with loss of contractility for the MV and a more dominant circular configuration through the cardiac cycle. All these associations show that abnormal human mitral geometry is intrinsically linked to mitral regurgitation (Lee et al., 2013, Mihaila, 2013, Sonne et al., 2009, Dal-Bianco and Levine, 2013).

The process of annular dilation differs for anterior and posterior circumferences in the human MV, with the anterior fibrous portion being less prone to dilation (McCarthy et al., 2010). Mathematically, this means that the inter-trigonal distance is not expected to change with mitral annular dilation (Calleja et al., 2015, Suri et al., 2009). The remaining 2/3 of the annulus (posterior annulus) is mainly muscular, dilating more easily (McCarthy et al., 2010). The anterior and posterior leaflet surface areas also increase with mitral regurgitation (Lee et al., 2013, Mihaila, 2013, Dal-Bianco and Levine, 2013, Senechal et al., 2012); however, no apparent trend in dilation concerning anterior vs posterior is present in the literature.

4.3 Geometrical changes in the subvalvular apparatus are related to type III dysfunction

Configurational changes of the subvalvular apparatus have a profound impact in MV function. A previous *in vitro* study using porcine specimens assessed the effect of different annulo-papillary lengths in MV coaptation, with different lengths leading to different MV states: not only increased

values are associated with damage to the valve, but a shortening in annulo-papillary lengths also induces diseased states (leaflet prolapse) (Espino et al., 2007). An optimum annulo-papillary length is therefore needed for proper MV coaptation. In fact, type III dysfunctions of the MV have been associated with geometrical alterations of the subvalvular apparatus. Clinical studies have shown that the PM suffer displacement in an attempt to attenuate the regurgitation effects (Lee et al., 2013, Silbiger, 2011): this is translated into increased inter-PM distance (Obase et al., 2016, Kim et al., 2014), which has been well correlated with increased regurgitant volume in patients with severe functional ischemic mitral regurgitation, as mathematically described by the equation below for end-systolic data ($R^2 = 0.84$, p-value < 0.01),

$$RV = -36.440 + 1.434 \cdot \upsilon, \tag{32}$$

where RV represents the regurgitant volume (in ml) and υ represents the inter-PM distance (in mm) (Jensen et al., 2010).

Type III dysfunction is also associated with increased left ventricular dimensions, which cause apical displacement of the PM. This leads to increased annulo-papillary lengths and chordae tendineae elongation (Obase et al., 2016). Previous clinical studies have connected PM displacement with the severity of mitral regurgitation: increased apical displacement of the posteromedial PM (PMPM) was associated with greater regurgitant volume (Jensen et al., 2010) and augmented tethering distance, characteristic of PM displacement, was correlated with increasing mitral regurgitation fraction at mid-systole (equation 33, R^2 stated as 0.64, p-value < 0.01) (Uemura et al., 2005).

$$M_{RF} = -60.990 + 3.583 \cdot TD, \tag{33}$$

where TD represents the PMPM tethering distance (in mm/m^2) and M_{RF} represents the mitral regurgitation fraction (as a percentage).

Another clinical study found independent associations between apical displacement of the PMPM and posterior displacement of the AL-PM with increasing tenting area, related to loss of systolic annular function and regurgitation (Yiu et al., 2000). However, the obtained data was too disperse to yield strong correlations amongst these parameters.

5. Future directions and recommendations for the use of morphometric information in mitral valve clinical analysis

This review paper focuses on grouping and briefly outlining the current best knowledge regarding MV morphometry by obtaining data from a range of different sources, including *in vitro*, *in vivo* and *in silico* studies. Quantitative data available has been analysed to derive further empirical mathematical relationships between dimensions. These can prove valuable to describe a healthy status of the MV, or can show the association between an abnormal valve shape and cases of dysfunction. It remains challenging to combine the morphometric information available in the literature to produce a coherent morphometric model of the human MV, based on mathematical correlations. Empirical relationships derived from direct correlations between dimensions and any relationships predicted analytically (or mathematically derived shapes) present with inherent differences. In addition, such correlations are derived from a specific imaging time frame, proving difficult to generalize these findings to the entire cardiac cycle.

Moreover, the use of different imaging modalities to obtain quantitative measurements, or the employment of different reference points, coordinate systems and anatomical landmarks, may lead to differing ranges for the same dimensions across studies. On the other hand, several imaging modalities present with lack of spatial resolution, therefore becoming difficult to accurately measure valvar dimensions. It also remains challenging to rigorously represent the subvalvular apparatus, as current *in vivo* imaging modalities are unable to properly capture the chordae and PM. These are the motivation behind the use of *ex vivo* data in computational models, as well as complete *ex vivo* animal geometries, which, in combination with micro CT imaging, allow for high resolution detail of all MV components (Khalighi et al., 2017, Khalighi et al., 2018, Bloodworth et al., 2017).

Computational modelling has been directed towards the study of MV function: while some studies have focused on normal physiological valve functioning (Domenichini and Pedrizzetti, 2015, Gao et al., 2017a, Votta et al., 2008, Wang and Sun, 2013), others have devoted towards diseased cases (Choi et al., 2016, Rim et al., 2013, Wenk et al., 2010) and surgical procedures (Ge et al., 2014, Rim et al., 2015, Rausch et al., 2017). The first geometrical models were based on idealized shapes of the MV, derived from literature data (Kunzelman et al., 1993, Salgo et al., 2002). However, since the accuracy of MV models is highly sensitive to valve geometry, patient-specific approaches have been preferred, with the MV apparatus being derived from medical images (Rim et al., 2013, Ge et al., 2014). Moreover, studies have devoted towards less invasive methodologies for the determination of mitral tissue properties in vivo, including leaflet strains (Rego et al., 2018). Faster and more efficient methods

to study MV function are becoming a reality; for example, a recent study has employed a complete human heart model (Baillargeon et al., 2014) to study ventricular dilation, its impact on the MV structure and its repair through annuloplasty (Rausch et al., 2017). This demonstrates the great potential of computational simulations to optimize medical intervention, develop tailored device designs and aid in treatment management. The use of a more complete set of morphometric information on the MV, such as the one described in this paper, may aid in this endeavour, which can then be useful to study the biomechanics associated with specific valvar shapes, in healthy and diseased ranges.

Declarations of interest: none

Ethics

The data obtained by the authors belongs to healthy volunteers recruited under the ethically approved research study "Exercise Capacity in Adults" with REC reference 13/NS/0034 and IRAS ID 127501.

Financial support

The creation of the database employed on our study was sponsored by the University of Aberdeen, under the research study "Exercise Capacity in Adults".

Authors' contributions

All authors were involved in the design of the study and have critically revised the manuscript. Individual contributions are as below:

Miss Diana Oliveira: Initial draft of the manuscript; gathering of morphometric mitral valve information from the current literature, for healthy and diseased cases; statistical analysis with published data; acquisition of mitral valve anatomic data and respective data analysis.

Dr Janaki Srinivasan: Acquisition of mitral valve anatomic data.

Dr Dana Dawson: Clinical guidance; recommendation of the clinical database to employ and decision on the sample to use.

Dr Keith Buchan: Surgical guidance; determination of relevant morphometric aspects of the mitral valve, including anatomic arrangements from the surgical point of view; advice on image sketches for the manuscript.

Dr Daniel Espino: Guidance on organization and presentation of information and data.

Prof Duncan Shepherd: Guidance on organization and presentation of information and data.

References

AL-ATABI, M., ESPINO, D. M., HUKINS, D. W. & BUCHAN, K. G. 2012. Biomechanical assessment of surgical repair of the mitral valve. *Proc Inst Mech Eng H,* 226**,** 275-87.

BAILLARGEON, B., REBELO, N., FOX, D. D., TAYLOR, R. L. & KUHL, E. 2014. The Living Heart Project: A robust and integrative simulator for human heart function. *Eur J Mech A Solids,* 48**,** 38-47.

BLOODWORTH, C. H. T., PIERCE, E. L., EASLEY, T. F., DRACH, A., KHALIGHI, A. H., TOMA, M., JENSEN, M. O., SACKS, M. S. & YOGANATHAN, A. P. 2017. Ex Vivo Methods for Informing Computational Models of the Mitral Valve. *Ann Biomed Eng,* 45**,** 496-507.

BOUMA, W. & GORMAN, R. C. 2019. Commentary: Three-dimensional P3 tethering angle at the heart of future surgical decision making in ischemic mitral regurgitation. *Journal of Thoracic and Cardiovascular Surgery,* 157**,** 1806-1807.

CALLEJA, A., POULIN, F., WOO, A., MEINERI, M., JEDRZKIEWICZ, S., VANNAN, M. A., RAKOWSKI, H., DAVID, T., TSANG, W. & THAVENDIRANATHAN, P. 2015. Quantitative Modeling of the Mitral Valve by Three-Dimensional Transesophageal Echocardiography in Patients Undergoing Mitral Valve Repair: Correlation with Intraoperative Surgical Technique. *J Am Soc Echocardiogr,* 28**,** 1083-92.

CARPENTIER, A. 1983. Cardiac valve surgery--the "French correction". *J Thorac Cardiovasc Surg,* 86**,** 323-37.

CARPENTIER, A., CHAUVAUD, S., FABIANI, J. N., DELOCHE, A., RELLAND, J., LESSANA, A., D'ALLAINES, C., BLONDEAU, P., PIWNICA, A. & DUBOST, C. 1980. Reconstructive surgery of mitral valve incompetence: ten-year appraisal. *J Thorac Cardiovasc Surg,* 79**,** 338-48.

CARPENTIER, A. F., LESSANA, A., RELLAND, J. Y., BELLI, E., MIHAILEANU, S., BERREBI, A. J., PALSKY, E. & LOULMET, D. F. 1995. The "physio-ring": an advanced concept in mitral valve annuloplasty. *Ann Thorac Surg,* 60**,** 1177-85; discussion 1185-6.

CASTILLO, J. G., SOLIS, J., GONZALEZ-PINTO, A. & ADAMS, D. H. 2011. [Surgical echocardiography of the mitral valve]. *Rev Esp Cardiol,* 64**,** 1169-81.

CHOI, A., MCPHERSON, D. D. & KIM, H. 2016. Biomechanical evaluation of the pathophysiologic developmental mechanisms of mitral valve prolapse: effect of valvular morphologic alteration. *Med Biol Eng Comput,* 54**,** 799-809.

CIARKA, A., BRAUN, J., DELGADO, V., VERSTEEGH, M., BOERSMA, E., KLAUTZ, R., DION, R., BAX, J. J. & VAN DE VEIRE, N. 2010. Predictors of mitral regurgitation recurrence in patients with heart failure undergoing mitral valve annuloplasty. *Am J Cardiol,* 106**,** 395-401.

COCHRAN, R. P. & KUNZELMAN, K. S. 1998. Effect of papillary muscle position on mitral valve function: relationship to homografts. *Ann Thorac Surg,* 66**,** S155-61.

CONG, T., GU, J., LEE, A. P., SHANG, Z., SUN, Y., SUN, Q., WEI, H., CHEN, N., SUN, S. & FU, T. 2018. Quantitative analysis of mitral valve morphology in atrial functional mitral

regurgitation using real-time 3-dimensional echocardiography atrial functional mitral regurgitation. *Cardiovasc Ultrasound,* 16**,** 13.
DAL-BIANCO, J. P. & LEVINE, R. A. 2013. Anatomy of the mitral valve apparatus: role of 2D and 3D echocardiography. *Cardiol Clin,* 31**,** 151-64.
DELGADO, V., TOPS, L. F., SCHUIJF, J. D., DE ROOS, A., BRUGADA, J., SCHALIJ, M. J., THOMAS, J. D. & BAX, J. J. 2009. Assessment of mitral valve anatomy and geometry with multislice computed tomography. *JACC Cardiovasc Imaging,* 2**,** 556-65.
DEORSOLA, L. & BELLONE, A. 2018. Coaptation Triangle and Golden Proportion in mitral valve anatomy. Does nature play with geometry? *Echocardiography,* 35**,** 30-38.
DOMENICHINI, F. & PEDRIZZETTI, G. 2015. Asymptotic Model of Fluid-Tissue Interaction for Mitral Valve Dynamics. *Cardiovasc Eng Technol,* 6**,** 95-104.
DUDZINSKI, D. M. & HUNG, J. 2014. Echocardiographic assessment of ischemic mitral regurgitation. *Cardiovasc Ultrasound,* 12**,** 46.
DUPLESSIS, L. A. & MARCHAND, P. 1964. The Anatomy of the Mitral Valve and Its Associated Structures. *Thorax,* 19**,** 221-7.
ECKERT, C. E., ZUBIATE, B., VERGNAT, M., GORMAN, J. H., 3RD, GORMAN, R. C. & SACKS, M. S. 2009. In vivo dynamic deformation of the mitral valve annulus. *Ann Biomed Eng,* 37**,** 1757-71.
ESPINO, D. M., SHEPHERD, D. E. & BUCHAN, K. G. 2007. Effect of mitral valve geometry on valve competence. *Heart Vessels,* 22**,** 109-15.
ESPINO, D. M., SHEPHERD, D. E., HUKINS, D. W. & BUCHAN, K. G. 2005. The role of Chordae tendineae in mitral valve competence. *J Heart Valve Dis,* 14**,** 603-9.
GAO, H., FENG, L., QI, N., BERRY, C., GRIFFITH, B. E. & LUO, X. 2017a. A coupled mitral valve-left ventricle model with fluid-structure interaction. *Med Eng Phys,* 47**,** 128-136.
GAO, H., QI, N., FENG, L., MA, X., DANTON, M., BERRY, C. & LUO, X. 2017b. Modelling mitral valvular dynamics-current trend and future directions. *Int J Numer Method Biomed Eng,* 33.
GARBI, M. & MONAGHAN, M. J. 2015. Quantitative mitral valve anatomy and pathology. *Echo Res Pract,* 2**,** R63-72.
GE, L., MORREL, W. G., WARD, A., MISHRA, R., ZHANG, Z., GUCCIONE, J. M., GROSSI, E. A. & RATCLIFFE, M. B. 2014. Measurement of mitral leaflet and annular geometry and stress after repair of posterior leaflet prolapse: virtual repair using a patient-specific finite element simulation. *Ann Thorac Surg,* 97**,** 1496-503.
GRBIC, S., EASLEY, T. F., MANSI, T., BLOODWORTH, C. H., PIERCE, E. L., VOIGT, I., NEUMANN, D., KREBS, J., YUH, D. D., JENSEN, M. O., COMANICIU, D. & YOGANATHAN, A. P. 2017. Personalized mitral valve closure computation and uncertainty analysis from 3D echocardiography. *Med Image Anal,* 35**,** 238-249.
GUNNAL, S. A., WABALE, R. N. & FAROOQUI, M. S. 2015. Morphological study of chordae tendinae in human cadaveric hearts. *Heart Views,* 16**,** 1-12.
HIRAKAWA, S., SASAYAMA, S., TOMOIKE, H., CROZATIER, B., FRANKLIN, D., MCKOWN, D. & ROSS, J., JR. 1977. In situ measurement of papillary muscle dynamics in the dog left ventricle. *Am J Physiol,* 233**,** H384-91.
IONASEC, R. I., VOIGT, I., GEORGESCU, B., WANG, Y., HOULE, H., VEGA-HIGUERA, F., NAVAB, N. & COMANICIU, D. 2010. Patient-specific modeling and quantification of the aortic and mitral valves from 4-D cardiac CT and TEE. *IEEE Trans Med Imaging,* 29**,** 1636-51.
JASSAR, A. S., VERGNAT, M., JACKSON, B. M., MCGARVEY, J. R., CHEUNG, A. T., FERRARI, G., WOO, Y. J., ACKER, M. A., GORMAN, R. C. & GORMAN, J. H. 2014. Regional Annular Geometry in Patients With Mitral Regurgitation: Implications for Annuloplasty Ring Selection. *Annals of Thoracic Surgery,* 97**,** 64-70.

JENSEN, H., JENSEN, M. O., SMERUP, M. H., RINGGAARD, S., SORENSEN, T. S., ANDERSEN, N. T., WIERUP, P., HASENKAM, J. M. & NIELSEN, S. L. 2010. Three-dimensional assessment of papillary muscle displacement in a porcine model of ischemic mitral regurgitation. *J Thorac Cardiovasc Surg,* 140**,** 1312-8.

JIANG, L., OWAIS, K., MATYAL, R., KHABBAZ, K. R., LIU, D. C., MONTEALEGRE-GALLEGOS, M., HESS, P. E. & MAHMOOD, F. 2014. Dynamism of the mitral annulus: a spatial and temporal analysis. *J Cardiothorac Vasc Anesth,* 28**,** 1191-7.

JIMENEZ, J. H., LIOU, S. W., PADALA, M., HE, Z., SACKS, M., GORMAN, R. C., GORMAN, J. H., 3RD & YOGANATHAN, A. P. 2007. A saddle-shaped annulus reduces systolic strain on the central region of the mitral valve anterior leaflet. *J Thorac Cardiovasc Surg,* 134**,** 1562-8.

JOLLEY, M. A., GHELANI, S. J., ADAR, A. & HARRILD, D. M. 2017. Three-Dimensional Mitral Valve Morphology and Age-Related Trends in Children and Young Adults with Structurally Normal Hearts Using Transthoracic Echocardiography. *J Am Soc Echocardiogr,* 30**,** 561-571.

KAISER, A. D., MCQUEEN, D. M. & PESKIN, C. S. 2019. Modeling the mitral valve. *Int J Numer Method Biomed Eng***,** e3240.

KHALIGHI, A. H., DRACH, A., BLOODWORTH, C. H. T., PIERCE, E. L., YOGANATHAN, A. P., GORMAN, R. C., GORMAN, J. H., 3RD & SACKS, M. S. 2017. Mitral Valve Chordae Tendineae: Topological and Geometrical Characterization. *Ann Biomed Eng,* 45**,** 378-393.

KHALIGHI, A. H., DRACH, A., GORMAN, R. C., GORMAN, J. H., 3RD & SACKS, M. S. 2018. Multi-resolution geometric modeling of the mitral heart valve leaflets. *Biomech Model Mechanobiol,* 17**,** 351-366.

KHALIGHI, A. H., REGO, B. V., DRACH, A., GORMAN, R. C., GORMAN, J. H., 3RD & SACKS, M. S. 2019. Development of a Functionally Equivalent Model of the Mitral Valve Chordae Tendineae Through Topology Optimization. *Ann Biomed Eng,* 47**,** 60-74.

KIM, K., KAJI, S., AN, Y., NISHINO, T., TANI, T., KITAI, T. & FURUKAWA, Y. 2014. Interpapillary muscle distance independently affects severity of functional mitral regurgitation in patients with systolic left ventricular dysfunction. *J Thorac Cardiovasc Surg,* 148**,** 434-40 e1.

KUNZELMAN, K. S., COCHRAN, R. P., CHUONG, C., RING, W. S., VERRIER, E. D. & EBERHART, R. D. 1993. Finite element analysis of the mitral valve. *J Heart Valve Dis,* 2**,** 326-40.

KUNZELMAN, K. S., COCHRAN, R. P., VERRIER, E. D. & EBERHART, R. C. 1994. Anatomic basis for mitral valve modelling. *J Heart Valve Dis,* 3**,** 491-6.

KUNZELMAN, K. S., EINSTEIN, D. R. & COCHRAN, R. P. 2007. Fluid-structure interaction models of the mitral valve: function in normal and pathological states. *Philos Trans R Soc Lond B Biol Sci,* 362**,** 1393-406.

LAM, J. H., RANGANATHAN, N., WIGLE, E. D. & SILVER, M. D. 1970. Morphology of the human mitral valve. I. Chordae tendineae: a new classification. *Circulation,* 41**,** 449-58.

LEE, A. P., HSIUNG, M. C., SALGO, I. S., FANG, F., XIE, J. M., ZHANG, Y. C., LIN, Q. S., LOOI, J. L., WAN, S., WONG, R. H., UNDERWOOD, M. J., SUN, J. P., YIN, W. H., WEI, J., TSAI, S. K. & YU, C. M. 2013. Quantitative analysis of mitral valve morphology in mitral valve prolapse with real-time 3-dimensional echocardiography: importance of annular saddle shape in the pathogenesis of mitral regurgitation. *Circulation,* 127**,** 832-41.

LEE, A. P., JIN, C. N., FAN, Y., WONG, R. H. L., UNDERWOOD, M. J. & WAN, S. 2017. Functional Implication of Mitral Annular Disjunction in Mitral Valve Prolapse: A Quantitative Dynamic 3D Echocardiographic Study. *JACC Cardiovasc Imaging,* 10**,** 1424-1433.

LEVACK, M. M., JASSAR, A. S., SHANG, E. K., VERGNAT, M., WOO, Y. J., ACKER, M. A., JACKSON, B. M., GORMAN, J. H., 3RD & GORMAN, R. C. 2012. Three-dimensional echocardiographic analysis of mitral annular dynamics: implication for annuloplasty selection. *Circulation,* 126**,** S183-8.

LOMHOLT, M., NIELSEN, S. L., HANSEN, S. B., ANDERSEN, N. T. & HASENKAM, J. M. 2002. Differential tension between secondary and primary mitral chordae in an acute in-vivo porcine model. *Journal of Heart Valve Disease,* 11**,** 337-345.

MACHINO-OHTSUKA, T., SEO, Y., ISHIZU, T., SATO, K., SUGANO, A., YAMAMOTO, M., HAMADA-HARIMURA, Y. & AONUMA, K. 2016. Novel Mechanistic Insights Into Atrial Functional Mitral Regurgitation-3-Dimensional Echocardiographic Study. *Circulation Journal,* 80**,** 2240-2248.

MANSI, T., VOIGT, I., GEORGESCU, B., ZHENG, X., MENGUE, E. A., HACKL, M., IONASEC, R. I., NOACK, T., SEEBURGER, J. & COMANICIU, D. 2012. An integrated framework for finite-element modeling of mitral valve biomechanics from medical images: application to MitralClip intervention planning. *Med Image Anal,* 16**,** 1330-46.

MARZILLI, M., SABBAH, H. N., LEE, T. & STEIN, P. D. 1980. Role of the papillary muscle in opening and closure of the mitral valve. *Am J Physiol,* 238**,** H348-54.

MCCARTHY, K. P., RING, L. & RANA, B. S. 2010. Anatomy of the mitral valve: understanding the mitral valve complex in mitral regurgitation. *Eur J Echocardiogr,* 11**,** i3-9.

MIHAILA, S., MURARU, D., CASABLANA, S., PELUSO, D., CUCCHINI, U., DEL BIANCO, L., VINEREANU, D., ILICETO, S., BADANO, L. 2013. Three-dimensional changes in mitral valve annulus geometry in organic and functional mitral regurgitation: insights for mitral valve repair. *Eur. Heart J.,* 34**,** 4751.

NIELSEN, S. L., TIMEK, T. A., GREEN, G. R., DAGUM, P., DAUGHTERS, G. T., HASENKAM, J. M., BOLGER, A. F., INGELS, N. B. & MILLER, D. C. 2003. Influence of anterior mitral leaflet second-order chordae tendineae on left ventricular systolic function. *Circulation,* 108**,** 486-491.

OBASE, K., WEINERT, L., HOLLATZ, A., FAROOQUI, F., ROBERTS, J. D., MINHAJ, M. M., TUNG, A., CHANEY, M., OTA, T., JEEVANANDAM, V., YOSHIDA, K., MOR-AVI, V. & LANG, R. M. 2016. Elongation of chordae tendineae as an adaptive process to reduce mitral regurgitation in functional mitral regurgitation. *Eur Heart J Cardiovasc Imaging,* 17**,** 500-9.

OKAMOTO, H., ITOH, Y. & NARA, Y. 2007. Geometric analysis of the anterior mitral leaflet and mitral valve orifice in cadaveric hearts. *Circ J,* 71**,** 1794-9.

OWAIS, K., MONTEALEGRE-GALLEGOS, M., JEGANATHAN, J., MATYAL, R., KHABBAZ, K. R. & MAHMOOD, F. 2016. Dynamic changes in the ischemic mitral annulus: Implications for ring sizing. *Ann Card Anaesth,* 19**,** 15-9.

PADALA, M., SACKS, M. S., LIOU, S. W., BALACHANDRAN, K., HE, Z. & YOGANATHAN, A. P. 2010. Mechanics of the mitral valve strut chordae insertion region. *J Biomech Eng,* 132**,** 081004.

PARK, J., GEIRSSON, A. & BONDE, P. N. 2019. Mathematical Blueprint of a Mitral Valve. *Semin Thorac Cardiovasc Surg*.

POUCH, A. M., VERGNAT, M., MCGARVEY, J. R., FERRARI, G., JACKSON, B. M., SEHGAL, C. M., YUSHKEVICH, P. A., GORMAN, R. C. & GORMAN, J. H. 2014. Statistical Assessment of Normal Mitral Annular Geometry Using Automated Three-Dimensional Echocardiographic Analysis. *Annals of Thoracic Surgery,* 97**,** 71-77.

PROT, V., SKALLERUD, B., SOMMER, G. & HOLZAPFEL, G. A. 2010. On modelling and analysis of healthy and pathological human mitral valves: two case studies. *J Mech Behav Biomed Mater,* 3**,** 167-77.

RANGANATHAN, N., LAM, J. H., WIGLE, E. D. & SILVER, M. D. 1970. Morphology of the human mitral valve. II. The valve leaflets. *Circulation,* 41**,** 459-67.

RAUSCH, M. K., BOTHE, W., KVITTING, J. P., SWANSON, J. C., INGELS, N. B., JR., MILLER, D. C. & KUHL, E. 2011. Characterization of mitral valve annular dynamics in the beating heart. *Ann Biomed Eng,* 39**,** 1690-702.

RAUSCH, M. K., ZOLLNER, A. M., GENET, M., BAILLARGEON, B., BOTHE, W. & KUHL, E. 2017. A virtual sizing tool for mitral valve annuloplasty. *Int J Numer Method Biomed Eng,* 33.

REGO, B. V., KHALIGHI, A. H., DRACH, A., LAI, E. K., POUCH, A. M., GORMAN, R. C., GORMAN, J. H., 3RD & SACKS, M. S. 2018. A noninvasive method for the determination of in vivo mitral valve leaflet strains. *Int J Numer Method Biomed Eng,* 34**,** e3142.

RIM, Y., CHOI, A., MCPHERSON, D. D. & KIM, H. 2015. Personalized Computational Modeling of Mitral Valve Prolapse: Virtual Leaflet Resection. *PLoS One,* 10**,** e0130906.

RIM, Y., MCPHERSON, D. D., CHANDRAN, K. B. & KIM, H. 2013. The effect of patient-specific annular motion on dynamic simulation of mitral valve function. *J Biomech,* 46**,** 1104-12.

SAHA, A. & ROY, S. 2018. Papillary muscles of left ventricle-Morphological variations and it's clinical relevance. *Indian Heart J,* 70**,** 894-900.

SAKAI, T., OKITA, Y., UEDA, Y., TAHATA, T., OGINO, H., MATSUYAMA, K. & MIKI, S. 1999. Distance between mitral anulus and papillary muscles: anatomic study in normal human hearts. *J Thorac Cardiovasc Surg,* 118**,** 636-41.

SALGO, I. S., GORMAN, J. H., 3RD, GORMAN, R. C., JACKSON, B. M., BOWEN, F. W., PLAPPERT, T., ST JOHN SUTTON, M. G. & EDMUNDS, L. H., JR. 2002. Effect of annular shape on leaflet curvature in reducing mitral leaflet stress. *Circulation,* 106**,** 711-7.

SEDRANSK, K. L., GRANDE-ALLEN, K. J. & VESELY, I. 2002. Failure mechanics of mitral valve chordae tendineae. *J Heart Valve Dis,* 11**,** 644-50.

SENECHAL, M., MICHAUD, N., MACHAALANY, J., BERNIER, M., DUBOIS, M., MAGNE, J., COUTURE, C., MATHIEU, P., BERTRAND, O. F. & VOISINE, P. 2012. Relation of mitral valve morphology and motion to mitral regurgitation severity in patients with mitral valve prolapse. *Cardiovasc Ultrasound,* 10**,** 3.

SHEN, X., WANG, T., CAO, X. & CAI, L. 2017. The geometric model of the human mitral valve. *PLoS One,* 12**,** e0183362.

SILBIGER, J. J. 2011. Mechanistic insights into ischemic mitral regurgitation: echocardiographic and surgical implications. *J Am Soc Echocardiogr,* 24**,** 707-19.

SONNE, C., SUGENG, L., WATANABE, N., WEINERT, L., SAITO, K., TSUKIJI, M., YOSHIDA, K., TAKEUCHI, M., MOR-AVI, V. & LANG, R. M. 2009. Age and body surface area dependency of mitral valve and papillary apparatus parameters: assessment by real-time three-dimensional echocardiography. *Eur J Echocardiogr,* 10**,** 287-94.

STEPHENS, S. E., LIACHENKO, S., INGELS, N. B., WENK, J. F. & JENSEN, M. O. 2017. High resolution imaging of the mitral valve in the natural state with 7 Tesla MRI. *Plos One,* 12.

STEVANELLA, M., MAFFESSANTI, F., CONTI, C. A., VOTTA, E., ARNOLDI, A., LOMBARDI, M., PARODI, O., CAIANI, E. G. & REDAELLI, A. 2011. Mitral Valve Patient-Specific Finite Element Modeling from Cardiac MRI: Application to an Annuloplasty Procedure. *Cardiovascular Engineering and Technology,* 2**,** 66-76.

STEVANELLA, M., VOTTA, E. & REDAELLI, A. 2009. Mitral valve finite element modeling: implications of tissues' nonlinear response and annular motion. *J Biomech Eng,* 131**,** 121010.

STONE, G. W., VAHANIAN, A. S., ADAMS, D. H., ABRAHAM, W. T., BORER, J. S., BAX, J. J., SCHOFER, J., CUTLIP, D. E., KRUCOFF, M. W., BLACKSTONE, E. H., GENEREUX, P., MACK, M. J., SIEGEL, R. J., GRAYBURN, P. A., ENRIQUEZ-SARANO, M., LANCELLOTTI, P., FILIPPATOS, G., KAPPETEIN, A. P. & MITRAL VALVE ACADEMIC RESEARCH, C. 2015. Clinical Trial Design Principles and Endpoint Definitions for Transcatheter Mitral Valve Repair and Replacement: Part 1: Clinical Trial Design Principles: A Consensus Document From the Mitral Valve Academic Research Consortium. *J Am Coll Cardiol,* 66**,** 278-307.

SUN, X., JIANG, Y., HUANG, G., HUANG, J., SHI, M., PANG, L. & WANG, Y. 2019. Three-dimensional mitral valve structure in predicting moderate ischemic mitral regurgitation

improvement after coronary artery bypass grafting. *J Thorac Cardiovasc Surg,* 157**,** 1795-1803 e2.

SURI, R. M., GREWAL, J., MANKAD, S., ENRIQUEZ-SARANO, M., MILLER, F. A., JR. & SCHAFF, H. V. 2009. Is the anterior intertrigonal distance increased in patients with mitral regurgitation due to leaflet prolapse? *Ann Thorac Surg,* 88**,** 1202-8.

TANG, Z., FAN, Y. T., WANG, Y., JIN, C. N., KWOK, K. W. & LEE, A. P. 2019. Mitral Annular and Left Ventricular Dynamics in Atrial Functional Mitral Regurgitation: A Three-Dimensional and Speckle-Tracking Echocardiographic Study. *J Am Soc Echocardiogr,* 32**,** 503-513.

TIMEK, T. A., NIELSEN, S. L., GREEN, G. R., DAGUM, P., BOLGER, A. F., DAUGHTERS, G. T., HASENKAM, J. M., INGELS, N. B. & MILLER, D. C. 2001. Influence of anterior mitral leaflet second-order chordae on leaflet dynamics and valve competence. *Annals of Thoracic Surgery,* 72**,** 535-540.

TOPILSKY, Y., VATURI, O., WATANABE, N., BICHARA, V., NKOMO, V. T., MICHELENA, H., LE TOURNEAU, T., MANKAD, S. V., PARK, S., CAPPS, M. A., SURI, R., PISLARU, S. V., MAALOUF, J., YOSHIDA, K. & ENRIQUEZ-SARANO, M. 2013. Real-time 3-dimensional dynamics of functional mitral regurgitation: a prospective quantitative and mechanistic study. *J Am Heart Assoc,* 2**,** e000039.

UEMURA, T., OTSUJI, Y., NAKASHIKI, K., YOSHIFUKU, S., MAKI, Y., YU, B., MIZUKAMI, N., KUWAHARA, E., HAMASAKI, S., BIRO, S., KISANUKI, A., MINAGOE, S., LEVINE, R. A. & TEI, C. 2005. Papillary muscle dysfunction attenuates ischemic mitral regurgitation in patients with localized basal inferior left ventricular remodeling: insights from tissue Doppler strain imaging. *J Am Coll Cardiol,* 46**,** 113-9.

VERONESI, F., CORSI, C., SUGENG, L., MOR-AVI, V., CAIANI, E. G., WEINERT, L., LAMBERTI, C. & LANG, R. M. 2009. A study of functional anatomy of aortic-mitral valve coupling using 3D matrix transesophageal echocardiography. *Circ Cardiovasc Imaging,* 2**,** 24-31.

VOTTA, E., CAIANI, E., VERONESI, F., SONCINI, M., MONTEVECCHI, F. M. & REDAELLI, A. 2008. Mitral valve finite-element modelling from ultrasound data: a pilot study for a new approach to understand mitral function and clinical scenarios. *Philos Trans A Math Phys Eng Sci,* 366**,** 3411-34.

WANG, Q. & SUN, W. 2013. Finite element modeling of mitral valve dynamic deformation using patient-specific multi-slices computed tomography scans. *Ann Biomed Eng,* 41**,** 142-53.

WARRAICH, H. J., CHAUDARY, B., MASLOW, A., PANZICA, P. J., PUGSLEY, J. & MAHMOOD, F. 2012. Mitral annular nonplanarity: correlation between annular height/commissural width ratio and the nonplanarity angle. *J Cardiothorac Vasc Anesth,* 26**,** 186-90.

WENK, J. F., ZHANG, Z., CHENG, G., MALHOTRA, D., ACEVEDO-BOLTON, G., BURGER, M., SUZUKI, T., SALONER, D. A., WALLACE, A. W., GUCCIONE, J. M. & RATCLIFFE, M. B. 2010. First finite element model of the left ventricle with mitral valve: insights into ischemic mitral regurgitation. *Ann Thorac Surg,* 89**,** 1546-53.

WILCOX, A. G., BUCHAN, K. G. & ESPINO, D. M. 2014. Frequency and diameter dependent viscoelastic properties of mitral valve chordae tendineae. *J Mech Behav Biomed Mater,* 30**,** 186-95.

YAMAURA, Y., ET AL. 2008. Three-Dimensional Echocardiographic Measurements of Distance Between Papillary Muscles and Mitral Annulus: Assessment With Three-Dimensional Quantification Software System. *J Echocardiogr,* 6**,** 67-73.

YIU, S. F., ENRIQUEZ-SARANO, M., TRIBOUILLOY, C., SEWARD, J. B. & TAJIK, A. J. 2000. Determinants of the degree of functional mitral regurgitation in patients with systolic left ventricular dysfunction: A quantitative clinical study. *Circulation,* 102**,** 1400-6.

ZHANG, F., KANIK, J., MANSI, T., VOIGT, I., SHARMA, P., IONASEC, R. I., SUBRAHMANYAN, L., LIN, B. A., SUGENG, L., YUH, D., COMANICIU, D. & DUNCAN, J. 2017. Towards patient-specific modeling of mitral valve repair: 3D transesophageal echocardiography-derived parameter estimation. *Med Image Anal,* 35**,** 599-609.

Supplementary Information:

1. Complete list of abbreviations and symbols used in equations

Table A

Abbreviation	Meaning
MV	Mitral valve
PM	Papillary muscle
3D	Three-dimensional
2D	Two-dimensional
AP	Antero-posterior
AL-PM	Anterolateral-posteromedial
A_C	Total annular circumference
A_{AC}	Anterior annular circumference
P_{AC}	Posterior annular circumference
AH	Annular height
IT	Inter-trigonal distance
AHCWR	Annular height to commissural width ratio
CI	Circularity index
CW	Commissural width
NPA	Non-planarity angle
A_{na}	2D annular area
A_{cord}	Anterior cord
P_{cord}	Posterior cord
A_{LA}	Anterior leaflet surface area
P_{LA}	Posterior leaflet surface area
EROA	Effective regurgitant orifice area
BV	Billow volume
RV	Regurgitant volume
M_{FR}	Mitral regurgitant fraction
TD	Tethering distance

Table B

Symbol	Mitral valve variable
γ	AL-PM distance
δ	Free edge length
ε	AHCWR
σ	AH to the AL-PM ratio
τ	AH to the AP ratio
λ	EROA
μ	Non-coaptation distance
υ	Inter-PM distance

675 *2. Methodology employed for derivation of prediction equations for mitral valve morphometry*
676
677 Aim: To perform linear and nonlinear regression analyses with published and obtained human
678 anatomical data in order to generate prediction equations for several mitral valve geometrical
679 parameters.

680

681 Steps taken:

682 Minitab 19 was employed for all regression analysis. Least-squares estimation was used to find
683 equations describing the relationship between two valve parameters at the time, with each data point
684 representing the value associated with one patient. This involved fitting different regression models to
685 the data, using the order presented in Table C (C_1, C_2 and C_3 are generic equation coefficients), and
686 evaluating the correlation coefficient R^2. This fitting process continued until the next fitting model did
687 not significantly increase the R^2. $R^2 < 0.5$ was associated with a poor correlation, $0.5 < R^2 < 0.8$ was
688 associated with a moderate correlation and $R^2 > 0.8$ was associated with a good correlation.

689

690 Table C

Regression model	Equation form
Linear	$y = C_1 + C_2 x$
Logarithmic	$y = C_1 + C_2 \ln x$
Exponential	$y = C_1 e^{C_2 x}$
Polynomial	$y = C_1 + C_2 x + C_3 x^2$

691

692 An analysis of variance to select an equation from the generated set was performed. This was not only
693 based on quality of fit, but also on the physical meaning of the prediction equations. This meant that
694 the values generated by each equation were compared to the clinical range and the standard-deviation
695 from literature data for validity. Therefore, high values of R^2 associated with a P-value < 0.01, together
696 with sensible 95% prediction intervals and consistent with the clinical ranges, indicated the equation
697 with best-fitting that could provide the best approximation to the data. When R^2 proved similar
698 amongst predictions, the simplest fit was chosen.

699 An example of the analysis of the physical meaning of prediction equations is explained below for
700 Equation 4 (P_{AC} predicted from A_C). During the generation of this equation, two models of best fit
701 were had into account: the linear regression ($R^2 = 0.93$, p-value < 0.01) and a 3rd degree polynomial
702 ($R^2 = 0.98$, p-value < 0.01). Both equations were tested with randomly generated values for the A_C

based on the standard-deviation from literature data and compared against the values obtained from the proportion found in the literature and present in Equation 1 of this manuscript (Figure A1).

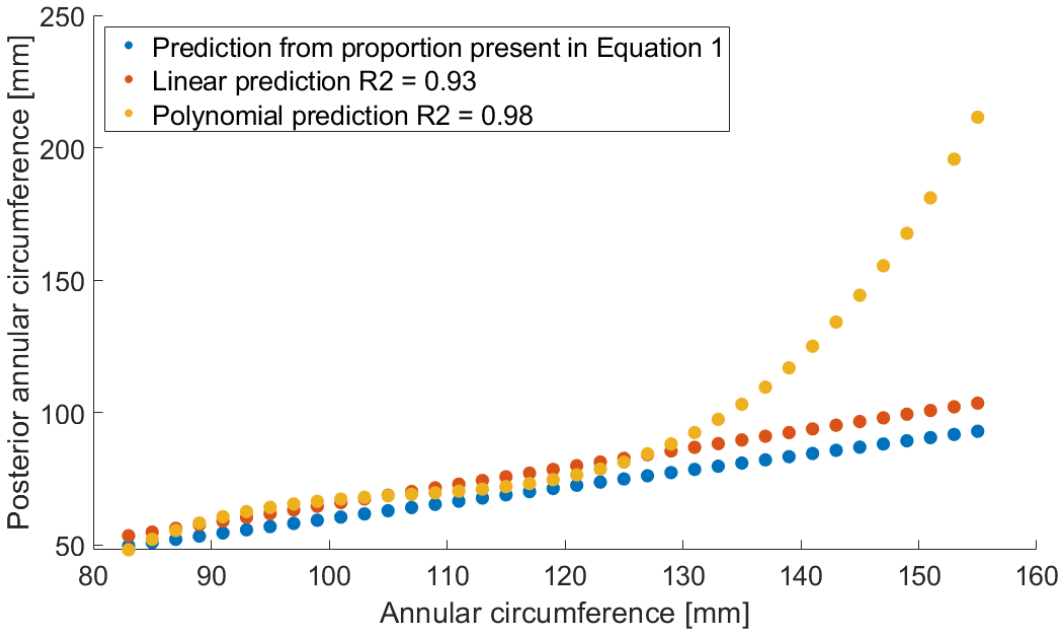

Figure A1. Linear (R^2 = 0.93, p-value < 0.01) and non-linear (R^2 = 0.98, p-value < 0.01) regression analysis performed on dimensions A_C and P_{AC} plotted against the prediction values obtained from Equation 1.

Despite having a higher R^2 than the linear equation, a 3rd degree polynomial equation greatly overestimates the P_{AC} for A_C values above 130 mm (when the annulus dilates), yielding non-physiological dimensions. Therefore, in this case, the linear prediction equation yields more sensible P_{AC} values.

3. *Prediction equations for mitral valve morphometry derived from literature and obtained clinical data*

Table D represents the prediction equations found for mitral valve morphometry, numbered as through the main text, and together with statistical analysis. x and y variables represent tested mitral valve dimensions. $p < 0.05$ indicates that the regression analysis was significant.

Table D

Equation number	Regression model	x	y	C_1	C_2	C_3	R^2	P-value
3	Linear	A_C [mm]	A_{AC} [mm]	4.137	0.305		0.72	< 0.01
4	Linear	A_C [mm]	P_{AC} [mm]	-4.137	0.695		0.93	< 0.01
5	Linear	γ [cm]	A_{AC} [cm]	2.500	0.420		0.66	< 0.01
6	Linear	γ [cm]	P_{AC} [cm]	4.400	1.200		0.91	< 0.01
10	Linear	A_C [mm]	δ [mm]	18.824	0.704		0.76	< 0.01
11	Linear	P_{AC} [mm]	δ [mm]	26.301	0.964		0.74	< 0.01
13	Linear	σ	NPA [º]	179.600	-163.900		0.70	< 0.01
14	Linear	σ	τ	0.027	0.970		0.78	< 0.01
15	Exponential	γ [mm]	IT [mm]	19.280	0.017		0.65	< 0.01
16	Linear	τ	NPA [º]	177.580	-142.880		0.64	< 0.01
17	Linear	A_{na} [mm^2]	AP [mm]	18.206	0.016		0.65	< 0.01
21	Linear	AP [mm]	A_{cord} [mm]	1.391	0.580		0.97	< 0.01
22	Linear	A_{cord} [mm]	P_{cord} [mm]	-1.279	0.667		0.82	< 0.01
23	Linear	A_C [mm]	A_{LA} [mm^2]	127.300	3.549		0.70	< 0.01
24	Linear	A_{AC} [mm]	A_{LA} [mm^2]	114.830	10.630		0.81	< 0.01
25	Linear	δ [mm]	A_{LA} [mm^2]	17.840	0.150		0.62	< 0.01
26	Linear	A_C [mm]	P_{LA} [mm^2]	65.749	4.262		0.85	< 0.01
27	Linear	P_{AC} [mm]	P_{LA} [mm^2]	113.250	5.798		0.82	< 0.01
28	Linear	P_{LA} [mm^2]	δ [mm]	14.797	0.152		0.75	< 0.01
29	Linear	A_{LA} [mm^2]	P_{LA} [mm^2]	53.285	0.914		0.71	< 0.01
30	Exponential	μ [mm]	λ [cm^2]	0.066	0.325		0.68	< 0.01
31	Polynomial	ε [%]	BV [ml]	10.000	-0.792	0.016	0.66	< 0.01
32	Linear	υ [mm]	RV [ml]	-36.440	1.434		0.84	< 0.01
33	Linear	TD [mm/m^2]	M_{RF} [%]	-60.990	3.583		0.58	< 0.01

4. *Example of regression analysis performed on data obtained from our 2D echocardiographic study*

Below is the regression analysis performed on data that we obtained from the database collected under the research study "Exercise Capacity in Adults" and from which prediction equations 5 (Figure A2) and 15 (Figure A3) were derived. Although the R^2 values for these equations are neither the highest nor the lowest, we chose them as an example of our regression analysis, because they derive from patient data collected by us, and not present in the literature.

On Figures A2 and A3 (a), the 95% confidence intervals shows us the two confidence boundaries where we can be 95% confident that that the true best-fit regression line is enclosed, while the 95% prediction intervals is the area in which 95% of all data points fall. On the other hand, each residual plot (Figures A2 and A3 (b)) shows how much the regression line vertically misses a data point, therefore displaying the difference between real and predicted response values. These residuals are randomly scattered above and below, showing that the assumptions of regression have been met. The standardized residuals are further away from zero for prediction equation 15 in comparison with equation 5, which shows that equation 5 better represents the real data and that equation 15 may generate outliers.

An additional normality test on the residuals was performed to verify the regression assumption that their distribution follows a Gaussian (or normal) distribution (Figures A2 and A3 (c)). We can observe that the residuals follow the ideal straight line. To further test for normality of data, an Anderson-Darling test was performed on the residuals, yielding p-values of 0.159 and 0.608 for equations 5 and 15, respectively. These show that there is not enough evidence for deviation of residuals from normality and therefore we can assume that the residuals follow a normal distribution.

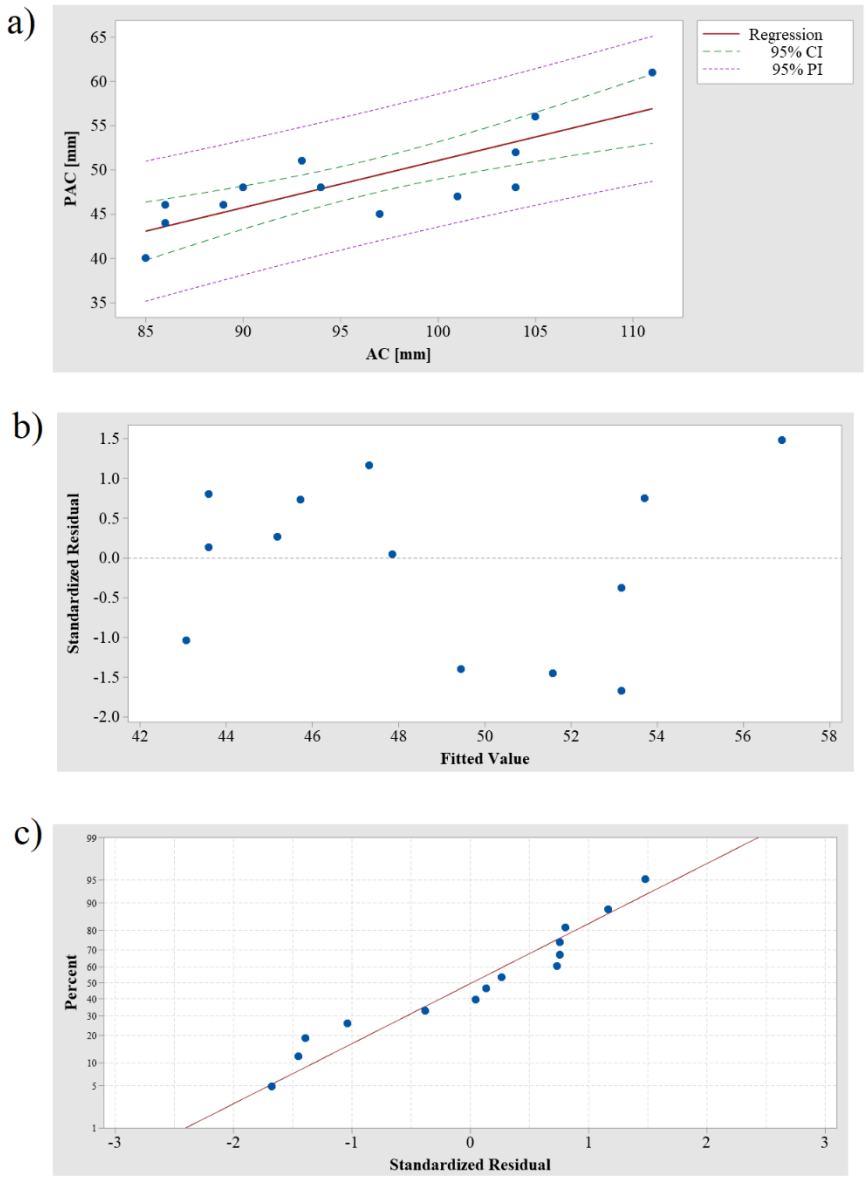

Figure A2. Regression analysis performed on dimensions A_C and P_{AC} (equation 5). a) Each blue marker represents data from each patient and linear regression (red line; $R^2 = 0.67$, p-value < 0.01) is presented, with 95% confidence (green, CI) and prediction (purple, PI) intervals; b) Residual plot, showing standardized residuals against fitted values; c) Normal probability plot of residuals, showing standardized residuals (x) identified with the percentiles (y) to which they correspond and displayed together with the ideal normal line (p-value = 0.159).

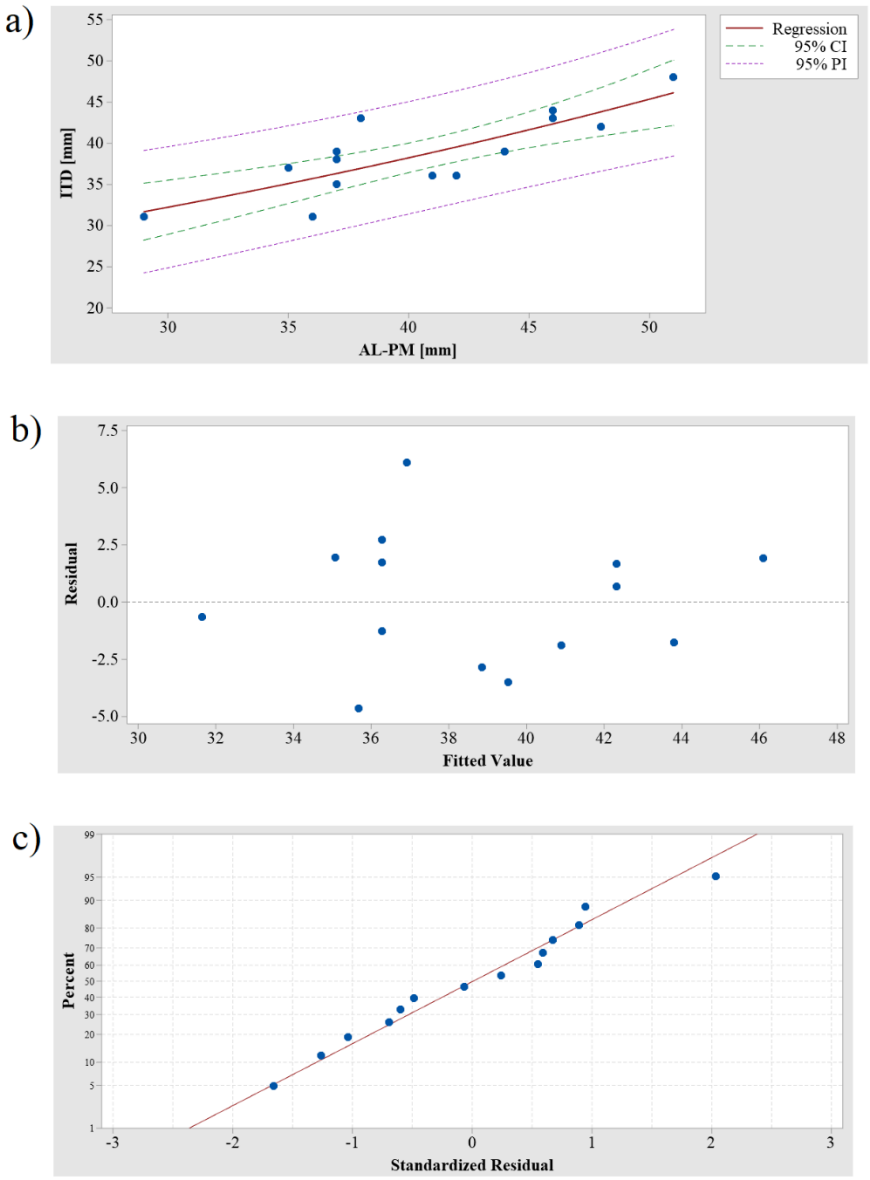

Figure A3. Regression analysis performed on dimensions AL-PM and inter-trigonal distance (ITD) (equation 15). a) Each blue marker represents data from each patient and exponential regression (red line; $R^2 = 0.66$, p-value < 0.01) is presented, with 95% confidence (green, CI) and prediction (purple, PI) intervals; b) Residual plot, showing standardized residuals against fitted values; c) Normal probability plot of residuals, showing standardized residuals (x) identified with the percentiles (y) to which they correspond and displayed together with the ideal normal line (p-value = 0.608).

Table legends

Table 1. Geometric variables of the MV and healthy and diseased (significant regurgitation) literature ranges ((Lee et al., 2013, Mihaila, 2013, Machino-Ohtsuka et al., 2016, Obase et al., 2016, Deorsola and Bellone, 2018, Jassar et al., 2014, Calleja et al., 2015, Sonne et al., 2009, Pouch et al., 2014, Jiang et al., 2014, Suri et al., 2009, Owais et al., 2016, Kunzelman et al., 1994, Ranganathan et al., 1970, Delgado et al., 2009, Dudzinski and Hung, 2014, Yamaura, 2008, Kim et al., 2014, Topilsky et al., 2013)). Dimensions obtained at: ⁜, early systole; *, mid-systole; †, end-systole; ‡, averaged over cardiac cycle; ※, ex vivo. Notes: AP, antero-posterior; CW, commissural width; AL-PM, anterolateral-posteromedial; NPA, non-planarity angle; IT, inter-trigonal; PM, papillary muscle; P1, posteromedial commissural scallop; P2, posterior middle scallop; P3, anterolateral commissural posterior scallop; AL, anterolateral; PM, posteromedial; ALPM, anterolateral papillary muscle; PMPM, posteromedial papillary muscle.

Figure legends

Figure 1. Porcine mitral valve apparatus: a) displays the anterior leaflet and chordae tendineae and b) focuses on the subvalvular apparatus, where chordae arise from both the PM and insert into the rough region of the posterior leaflet.

Figure 2. Human MV leaflet tissue areas. Notes: C, clear zone; R, rough zone; B, basal zone.

Figure 3. Atrial and lateral views of a mitral valve schematic model based upon nine landmarks. The annulus, anterior and posterior leaflets and papillary muscle tips can be observed.

Figure 4. Atrial (a) and lateral (b) views of important mitral annular dimensions. Notes: AV, aortic valve; LT, left trigone; RT, right trigone; P1, P2, P3, posterior leaflet scallops; AL-PM diameter, anterolateral-posteromedial diameter; AP, antero-posterior distance; CW, commissural width; IT, inter-trigonal distance.

Figure 5. Circle representing the annulus, according to Okamoto et al. (2007), with relevant dimensions highlighted. Notes: LT, left trigone; RT, right trigone; AL-PM diameter, anterolateral-posteromedial diameter; CW, commissural width; IT distance, inter-trigonal distance; θTg, trigonal angle; θCom, commissural angle.

Figure 6. Hyperboloids representing the mitral valve saddle shape and defined by equation 11 (Park et al., 2019) are displayed, created upon literature values for CW (33.3 mm), AP diameter (28 mm), AL-PM diameter (31 mm) and AHCWR (0.237). We can observe different commissural heights (b) and posterior annular depth (c) in comparison with a pure hyperboloid (a), given by changes in transformation parameters.

Figure 7. Coaptation triangle. The tenting height divides the base of the triangle (AP diameter) into two segments – the anterior and the posterior cords. Notes: α_A, anterior leaflet angle; α_P, posterior leaflet angle.

Figure 8. Parameters of human MV leaflet geometry, with an extended (a) and closed (b) leaflet representation. Notes: A-B, anterolateral commissure; B-C, anterior leaflet; C-D, posteromedial

commissure; D-A', posterior leaflet; D-E, posteromedial commissural scallop (P1); E-F, middle scallop (P2); F-A', anterolateral commissural scallop (P3).

Figure 9. Measurements describing PM morphology. Notes: ALPM, anterolateral PM; PMPM, posteromedial PM.

Figure 10. Distances between PM tips and o'clock points of mitral annulus, in axial (left) and isometric (right) views (adapted from (Sakai et al., 1999, Yamaura, 2008)). Notes: ALPM, anterolateral PM; PMPM, posteromedial PM; 0 o'clock, midpoint of the anterior annular circumference; 2 o'clock, right trigone; 10 o'clock, left trigone; 4 o'clock, separation of posterior and middle scallops of posterior leaflet; 8 o'clock, separation of anterior and middle scallops of posterior leaflet.

Figure 11. Axial view of C-shape representation for the PMs, as present in the literature and suggested by expert surgeons, as well as a simplified depiction of chordae tendineae insertion patterns. Blue, green and orange chordae are those inserting into the anterior leaflet, posterior leaflet and paracommissural zones, respectively.

Figure 12. Example of Reeb graph employed to characterize chordae tendineae topology in Khalighi et al. (2017), illustrating the connectivity between branches. Green, blue and orange vertices correspond to chordal origin (at the PM level), bifurcation points and insertion points into the leaflets, respectively.

Figure 13. Hyperboloids representing: a) a mitral annular normal saddle configuration; b) a configuration associated with type I dysfunction, defined as in Park et al (Park et al., 2019). The first configuration was created with the dimensions mentioned on Figure 6 and the diseased one upon literature values for CW (42.2 mm), AP diameter (38.8 mm), AL-PM diameter (39 mm) and AHCWR (0.132).

Figure A1. Linear ($R2 = 0.93$, p-value < 0.01) and non-linear ($R2 = 0.98$, p-value < 0.01) regression analysis performed on dimensions AC and PAC plotted against the prediction values obtained from Equation 1.

Figure A2. Regression analysis performed on dimensions AC and PAC. a) Each blue marker represents data from each patient and linear regression (red line; $R2 = 0.67$, p-value < 0.01) is presented, with 95% confidence (green, CI) and prediction (purple, PI) intervals; b) Residual plot, showing standardized residuals against fitted values; c) Normal probability plot of residuals, showing standardized residuals (x) identified with the percentiles (y) to which they correspond and displayed together with the ideal normal line (p-value = 0.159).

Figure A3. Regression analysis performed on dimensions AL-PM and inter-trigonal distance (ITD). a) Each blue marker represents data from each patient and exponential regression (red line; $R2 = 0.66$, p-value < 0.01) is presented, with 95% confidence (green, CI) and prediction (purple, PI) intervals; b) Residual plot, showing standardized residuals against fitted values; c) Normal probability plot of residuals, showing standardized residuals (x) identified with the percentiles (y) to which they correspond and displayed together with the ideal normal line (p-value = 0.608).